CHAPTER

SIX

CONTROL SYSTEM DESIGN CASE STUDIES

6.1 INTRODUCTION

This chapter is devoted to a series of case studies showing applications of modern control theory to chemical, petroleum, and metallurgical processes. For each problem, one or more of the techniques discussed in earlier chapters is used, and the performance of the resulting design is compared with more conventional approaches. It is hoped that this set of example problems will stimulate the reader to further applications in the real world of the process industries.

6.2 CONTROL OF A MULTI-SIDESTREAM DISTILLATION COLUMN*

The goal of this case study is to develop a control strategy for the multi-sidestream distillation column shown in Fig. 6.1. The compositions of the overhead and two sidestreams are the output variables y_1, y_2, y_3, and the drawoff rates of these streams constitute the manipulated variables u_1, u_2, u_3. Although one could formulate a very high-order time-domain model of the column involving concentrations and temperatures on every tray, this is not usually the best approach for process control design. As noted in Sec. 3.2, it is often possible to fit a linear

* This case study was carried out by Lance Lauerhass, Paul Noble, Larry Biegler, and Tunde Ogunnaike as a project in the graduate course in Advanced Process Control at the University of Wisconsin.

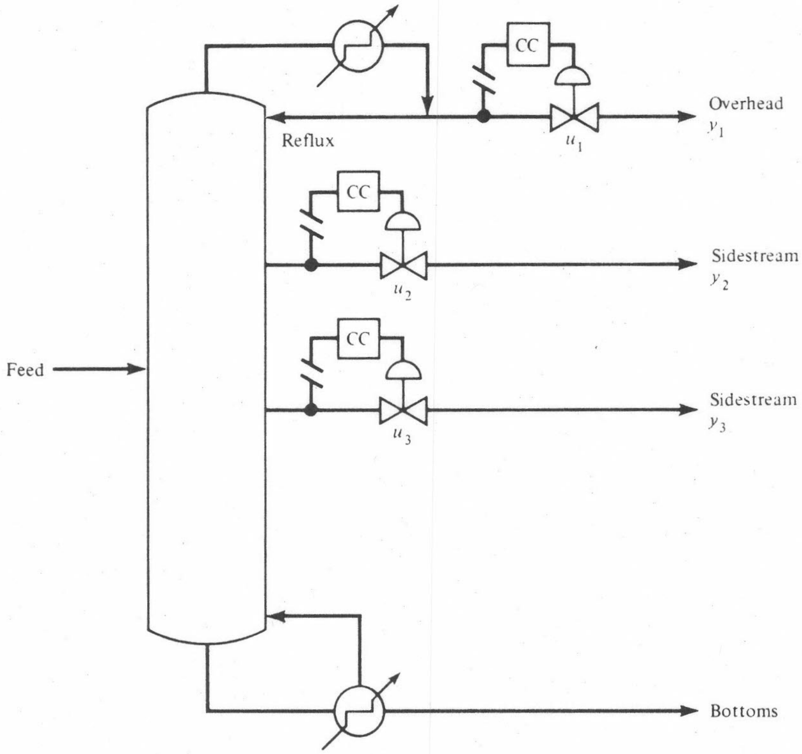

Figure 6.1 Distillation column schematic.

transfer function model to the observed sidestream composition dynamics through step- or frequency-response experiments. We shall assume this has been done in the present case, yielding the open-loop transfer function

$$\bar{\mathbf{y}}(s) = \mathbf{G}(s)\bar{\mathbf{u}}(s) \tag{6.2.1}$$

where

$$\mathbf{G}(s) = \begin{bmatrix} \frac{0.7}{1+9s} & 0 & 0 \\ \frac{2.0}{1+8s} & \frac{0.4}{1+6s} & 0 \\ \frac{2.3}{1+10s} & \frac{2.3}{1+8s} & \frac{2.1}{1+7s} \end{bmatrix} \tag{6.2.2}$$

Very often the experimentally determined transfer function $\mathbf{G}(s)$ includes pure time delays in some of the elements; however, we shall assume these are so small as to be negligible in the present case.

The present control scheme for the column consists of three single-loop controllers as shown in Fig. 6.2. For each loop, the composition y_i is measured and used in a PI controller to adjust the flow rate u_i. Experience has shown that

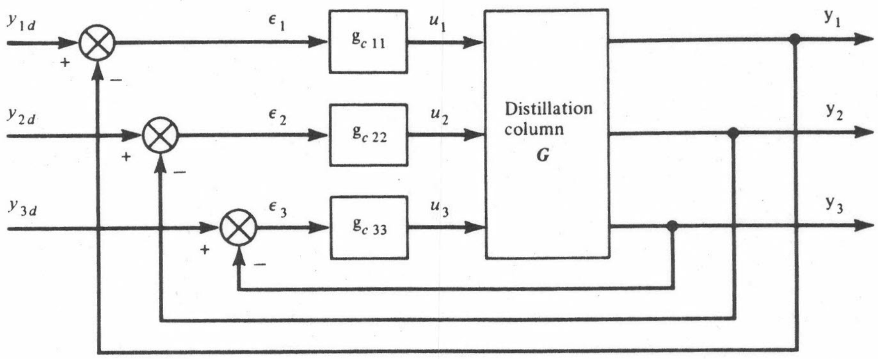

Figure 6.2 Multiple single-loop control for the distillation column.

there are two major operating difficulties with this present control system:

1. The response to disturbances is poor, yielding steady-state offset and oscillations.
2. Changing the set point in any one variable causes the other variables to go off specification and to oscillate.

To illustrate these problems, consider Fig. 6.3, which shows the response of three single-loop proportional controllers to set-point changes

$$\bar{\mathbf{y}}_d = \begin{bmatrix} 0.05 \\ -0.05 \\ 0.02 \end{bmatrix} \tag{6.2.3}$$

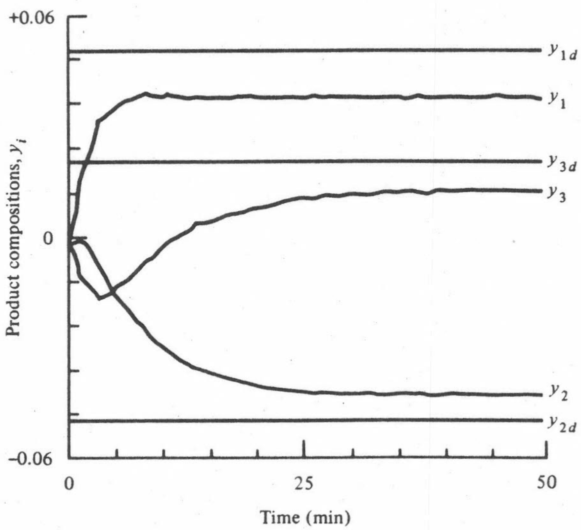

Figure 6.3 Product compositions after a set-point change (proportional control with $k_{c_{11}} = 5$, $k_{c_{22}} = 20$, $k_{c_{33}} = 20$).

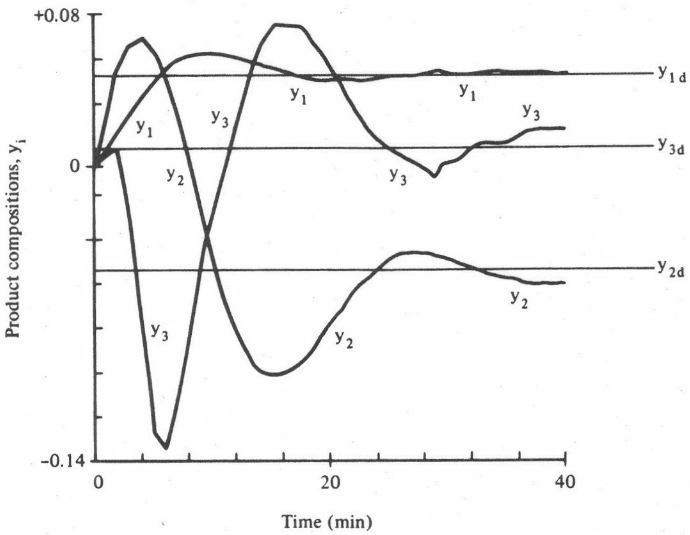

Figure 6.4 Product compositions after a set-point change (proportional plus integral control with $k_{c_u} = 2$, $\tau_i = 2$).

while Fig. 6.4 illustrates the response with three proportional plus integral controllers. With only proportional control (Fig. 6.3), both set-point changes and disturbances cause large offsets. When integral action is added in an effort to prevent offsets, the three controllers fight one another, causing persistent oscillations (Fig. 6.4). In this case study, two control strategies designed to eliminate these difficulties shall be evaluated.

Set-Point Compensation

In some distillation towers with multiple products, the effect of disturbances is minor and the principal difficulties arise due to frequent set-point changes. As discussed in Chap. 3, the simple techniques of set-point compensation can correct many of these types of difficulties. Recall from Sec. 3.2 that the addition of set-point compensation modifies Fig. 6.2 to the control scheme shown in Fig. 6.5. The closed-loop transfer function becomes

$$\bar{\mathbf{y}} = (\mathbf{I} + \mathbf{G}\mathbf{G}_c)^{-1}\mathbf{G}\mathbf{G}_c\mathbf{S}\hat{\mathbf{y}}_d \qquad (3.2.94)$$

where the controller matrix is

$$\mathbf{G}_c = \begin{bmatrix} g_{c11} & 0 & 0 \\ 0 & g_{c22} & 0 \\ 0 & 0 & g_{c33} \end{bmatrix}$$

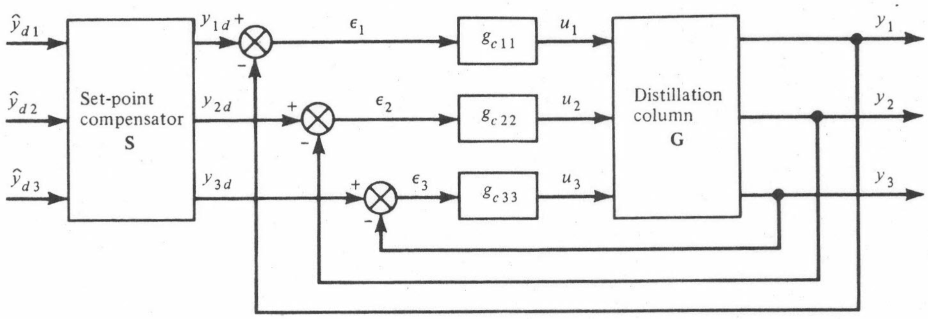

Figure 6.5 Set-point compensator added to multiple single-loop control.

and the set-point compensator

$$\mathbf{S} = \begin{bmatrix} S_{11} & S_{12} & S_{13} \\ S_{21} & S_{22} & S_{23} \\ S_{31} & S_{32} & S_{33} \end{bmatrix}$$

is to be chosen to make

$$(\mathbf{I} + \mathbf{G}\mathbf{G}_c)^{-1}\mathbf{G}\mathbf{G}_c\mathbf{S} = \mathbf{I} \qquad (6.2.4)$$

at steady state. Thus, if the single-loop controllers are proportional controllers $g_{cii} = K_{cii}$, $i = 1, 2, 3$, then

$$\mathbf{S} = \begin{bmatrix} \dfrac{1.43}{K_{c11}} + 1 & 0 & 0 \\ -\dfrac{7.14}{K_{c22}} & \dfrac{2.5}{K_{c22}} + 1 & 0 \\ \dfrac{6.26}{K_{c33}} & -\dfrac{2.74}{K_{c33}} & \dfrac{0.48}{K_{c33}} + 1 \end{bmatrix} \qquad (6.2.5)$$

satisfies Eq. (6.2.4). The performance of this compensator is discussed below.

Noninteracting Control

A second control strategy to be evaluated is multivariable noninteracting control, shown in Fig. 6.6. It may be implemented using single-loop controllers, but the signals from these controllers must be sent to decoupling operators to accomplish the noninteractive control. Recall from Chap. 3 that the closed-loop transfer function for the structure in Fig. 6.6 is

$$\bar{\mathbf{y}} = (\mathbf{I} + \mathbf{G}\mathbf{G}_I\mathbf{G}_c)^{-1}\mathbf{G}\mathbf{G}_I\mathbf{G}_c\bar{\mathbf{y}}_d \qquad (3.2.81)$$

and $\mathbf{G}_I$ must be chosen to make

$$\mathbf{T} = (\mathbf{I} + \mathbf{G}\mathbf{G}_I\mathbf{G}_c)^{-1}\mathbf{G}\mathbf{G}_I\mathbf{G}_c \qquad (3.2.82)$$

a diagonal matrix.

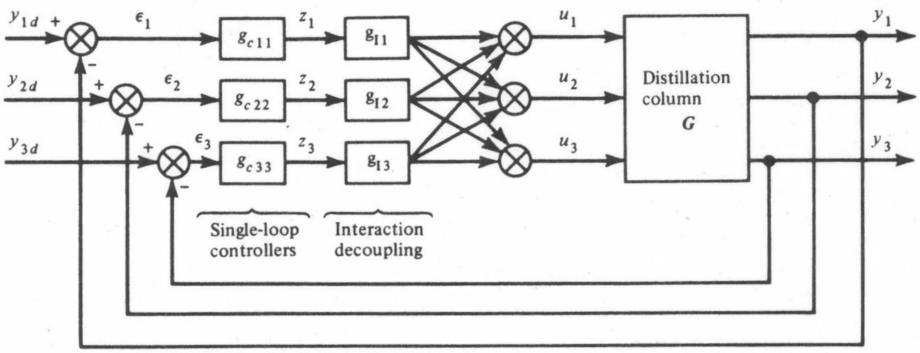

Figure 6.6 Noninteracting multivariable feedback control.

For the simple case of *steady-state compensation*, which eliminates steady-state interactions, one could choose to let

$$\mathbf{G}_I = (\mathbf{G}_{ss}^{-1})\mathrm{diag}\,\mathbf{G}_{ss} \tag{3.2.85}$$

where

$$\mathbf{G}_{ss} = \lim_{s\to 0}\mathbf{G}(s) = \begin{bmatrix} 0.7 & 0 & 0 \\ 2.0 & 0.4 & 0 \\ 2.3 & 2.3 & 2.1 \end{bmatrix}$$

However, in this example, we shall be even more demanding and require that perfect steady-state compensation be accomplished; i.e., we must choose

$$\mathbf{G}_I = (\mathbf{G}^{-1})_{ss} = \begin{bmatrix} 1.43 & 0 & 0 \\ -7.14 & 2.5 & 0 \\ 6.26 & -2.74 & 0.48 \end{bmatrix}$$

Furthermore, we could pursue the even more ambitious goal of perfectly compensating for dynamic interactions. For this example, such a "perfect" dynamic compensator would take the form

$$\mathbf{G}_I = \mathbf{G}^{-1} = \begin{bmatrix} 1.43(1+9s) & 0 & 0 \\ \dfrac{-7.14(1+9s)(1+6s)}{(1+8s)} & 2.50(1+6s) & 0 \\ \left\{\dfrac{7.82(1+9s)(1+6s)(1+7s)}{(1+8s)^2} \quad \dfrac{-1.56(1+9s)(1+7s)}{1+10s}\right\} & \dfrac{-2.74(1+6s)(1+7s)}{1+8s} & 0.48(1+7s) \end{bmatrix} \tag{6.2.6}$$

This compensator may be implemented by noting that

$$\mathbf{u} = \mathbf{G}_I \mathbf{G}_c \boldsymbol{\epsilon} \tag{6.2.7}$$

determines the desired control action. If $\mathbf{G}_c$ represents an actual set of three controllers as shown in Fig. 6.6, then

$$z_1 = g_{c11}\epsilon_1 \qquad z_2 = g_{c22}\epsilon_2 \qquad z_3 = g_{c33}\epsilon_3 \tag{6.2.8}$$

and

$$\mathbf{u} = \mathbf{G}_I \mathbf{z} \tag{6.2.9}$$

is the operation which must be carried out to accomplish this dynamic decoupling. From Eq. (6.2.6), this operation requires that

$$u_1(s) = 1.43(1 + 9s)z_1(s) \tag{6.2.10}$$

$$u_2(s) = \frac{-7.14(1 + 9s)(1 + 6s)}{1 + 8s} z_1(s) + 2.50(1 + 6s)z_2(s) \tag{6.2.11}$$

$$u_3(s) = \left[\frac{7.82(1 + 9s)(1 + 6s)(1 + 7s)}{(1 + 8s)^2} - \frac{1.56(1 + 9s)(1 + 7s)}{1 + 10s}\right] z_1(s)$$

$$- \frac{2.74(1 + 6s)(1 + 7s)}{1 + 8s} z_2(s) + 0.48(1 + 7s)z_3(s) \tag{6.2.12}$$

Transforming these expressions to the time domain, one obtains

$$u_1(t) = 1.43\left[z_1(t) + 9\frac{dz_1(t)}{dt}\right] \tag{6.2.13}$$

$$u_2(t) = -7.14\left[6.75\frac{dz_1}{dt} + 1.03z_1 - 0.0039\int_0^t \exp\left(-\frac{t - \tau}{8}\right)z_1(\tau)\,d\tau\right]$$

$$+2.50\left[z_2(t) + 6\frac{dz_2}{dt}\right] \tag{6.2.14}$$

$$u_3(t) = 7.82\left[5.91\frac{dz_1}{dt} + 1.01z_1 - (0.000488 + 0.0000610t)\right.$$

$$\left.\times \int_0^t \exp\left(-\frac{t - \tau}{8}\right)z_1(\tau)\,d\tau + 0.0000610\int_0^t \exp\left(-\frac{t - \tau}{8}\right)\tau z_1(\tau)\,d\tau\right]$$

$$-1.56\left[6.3\frac{dz_1}{dt} + 0.97z_1 + 0.003\int_0^t \exp\left(-\frac{t - \tau}{10}\right)z_1(\tau)\,d\tau\right]$$

$$-2.74\left[5.25\frac{dz_2}{dt} + 9.69z_2 + 0.0022\int_0^t \exp\left(-\frac{t - \tau}{8}\right)z_2(\tau)\,d\tau\right]$$

$$+0.48\left[z_3(t) + 7\frac{dz_3}{dt}\right] \tag{6.2.15}$$

This integration and differentiation of the signal $z_i(t)$ can clearly be implemented either with analog circuitry or by a real-time digital controller. For the case of DDC, Eq. (6.2.8) would also be carried out by the digital computer.

Control System Performance Testing

In order to test the performance of these two control schemes when implemented on the process control digital computer, the distillation column was simulated on the analog computer and the control algorithms programmed to respond in real time on the digital computer. The information flow is shown in Fig. 6.7, and the analog circuit diagram representing the column is presented in Fig. 6.8.

Before proceeding further to test these algorithms, it is useful to investigate the *controllability* of the column. The transfer function model [Eq. (6.2.1)] may be easily put into the time domain to yield equations of the form

$$\frac{d\mathbf{x}}{dt} = \mathbf{Ax} + \mathbf{Bu} \tag{6.2.16}$$

$$\mathbf{y} = \mathbf{Cx} \tag{6.2.17}$$

where

$$\mathbf{x} = \begin{bmatrix} x_1 \\ x_2 \\ \vdots \\ x_6 \end{bmatrix}$$

$$\mathbf{A} = \begin{bmatrix} -0.111 & 0 & 0 & 0 & 0 & 0 \\ 0 & -0.125 & 0 & 0 & 0 & 0 \\ 0 & 0 & -0.167 & 0 & 0 & 0 \\ 0 & 0 & 0 & -0.1 & 0 & 0 \\ 0 & 0 & 0 & 0 & -0.125 & 0 \\ 0 & 0 & 0 & 0 & 0 & -0.143 \end{bmatrix}$$

$$\mathbf{B} = \begin{bmatrix} 1 & 0 & 0 \\ 1 & 0 & 0 \\ 0 & 1 & 0 \\ 1 & 0 & 0 \\ 0 & 1 & 0 \\ 0 & 0 & 1 \end{bmatrix} \qquad \mathbf{C} = \begin{bmatrix} 1 & 0 & 0 & 0 & 0 & 0 \\ 0 & 1 & 1 & 0 & 0 & 0 \\ 0 & 0 & 0 & 1 & 1 & 1 \end{bmatrix} \tag{6.2.18}$$

The output controllability matrix, which is

$$\mathbf{L}_y = [\mathbf{CB} \,\vdots\, \mathbf{CAB} \,\vdots\, \ldots \,\vdots\, \mathbf{CA}^5\mathbf{B}] \tag{6.2.19}$$

clearly has rank 3 because

$$\mathbf{CB} = \begin{bmatrix} 1 & 0 & 0 \\ 1 & 1 & 0 \\ 1 & 1 & 1 \end{bmatrix} \tag{6.2.20}$$

is nonsingular; thus the column is *completely controllable*.

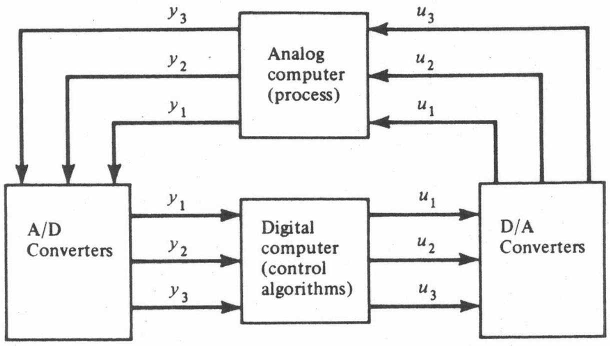

Figure 6.7 Digital computer control of the simulated process.

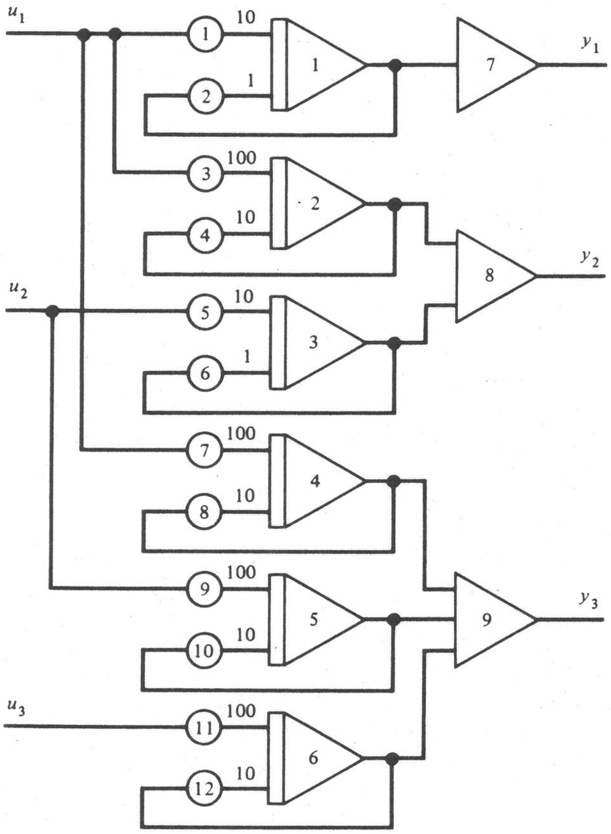

Figure 6.8 Analog circuit diagram.

The *set-point compensation* algorithm shown in Fig. 6.5 was applied for the same conditions as for Fig. 6.3 [i.e., with three proportional controllers and a set-point change given by Eq. (6.2.3)]. The dynamic response of the column, shown in Fig. 6.9, is much improved over the uncompensated case, showing rapid attainment of steady state, with very little offset and no oscillations. Further experiments confirmed that good performance for set-point changes

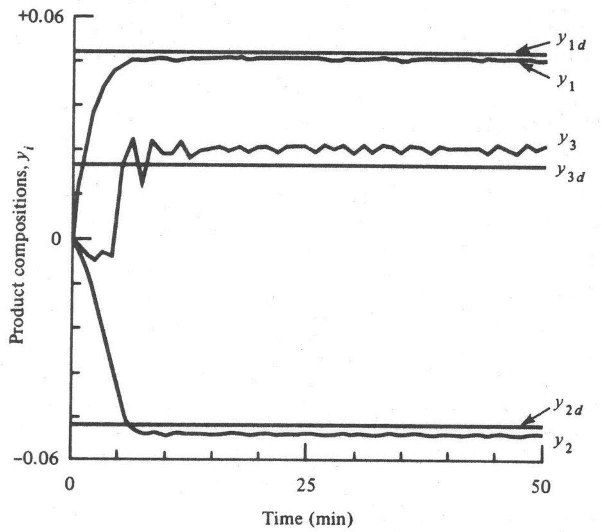

Figure 6.9 Product compositions after a set-point change (set-point compensator used with proportional controllers, same conditions as for Fig. 6.3).

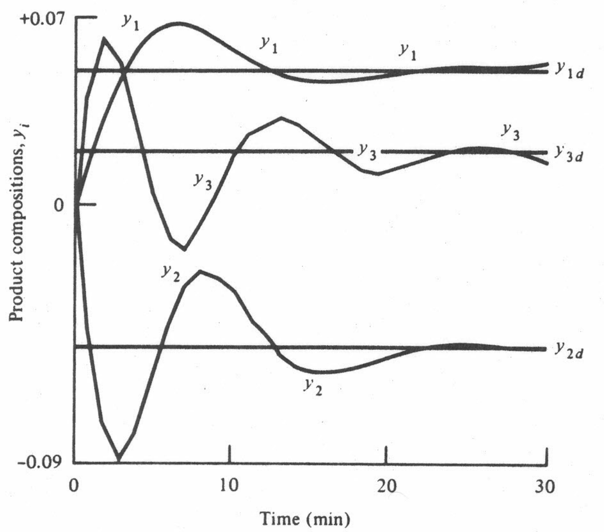

Figure 6.10 Product compositions after a set-point change (steady-state decoupling together with proportional plus integral controllers, $k_{c_{ii}} = 2.0$, $\tau_i = 2.0$).

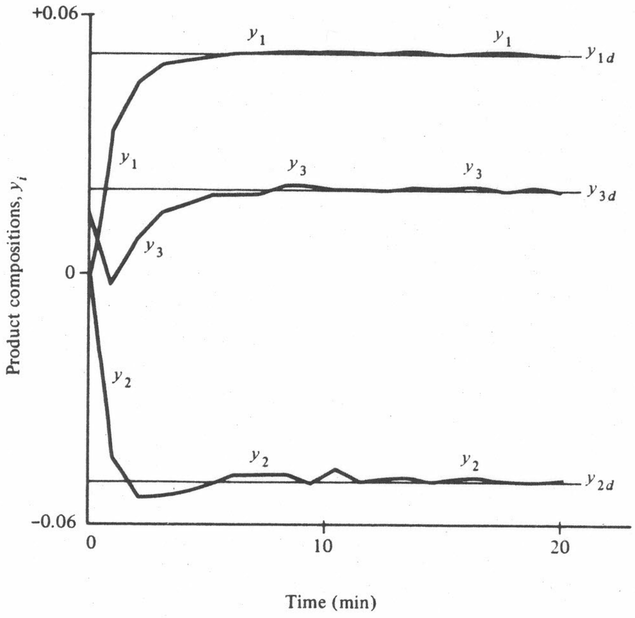

Figure 6.11 Product compositions after a set-point change (dynamic decoupling together with proportional plus integral controllers, $k_{c_u} = 0.25$, $\tau_i = 0.5$).

should be expected with this control scheme. Unfortunately, the set-point compensator does not help in the case of disturbances because it is not contained in the feedback loop.

To improve the control system performance in the face of disturbances, both steady-state and dynamic noninteracting control schemes were tested. Figure 6.10 shows the effect of adding *steady-state compensation* for the conditions of Fig. 6.4. Notice that even though there are still some oscillations, they are smaller in amplitude and settle faster than the response shown in Fig. 6.4. By adding *dynamic compensation*, the response is improved even more dramatically, as shown in Fig. 6.11. The settling time without any compensation (Fig. 6.4) is on the order of 50 to 60 min, while for steady-state decoupling (Fig. 6.10) this drops to ~25 min. What is even more impressive is that the dynamic decoupling controller produces a settling time of only about 6 min—an order-of-magnitude improvement over multiple single-loop control.

Evaluation

Although all the new control schemes worked better than the multiple single-loop controllers, the dynamic noninteracting controller performed best and handled both disturbances and set-point changes. The set-point compensation algorithm is much simpler to implement and gives good response to set-point changes, but cannot respond to disturbances. Thus if one does not wish to

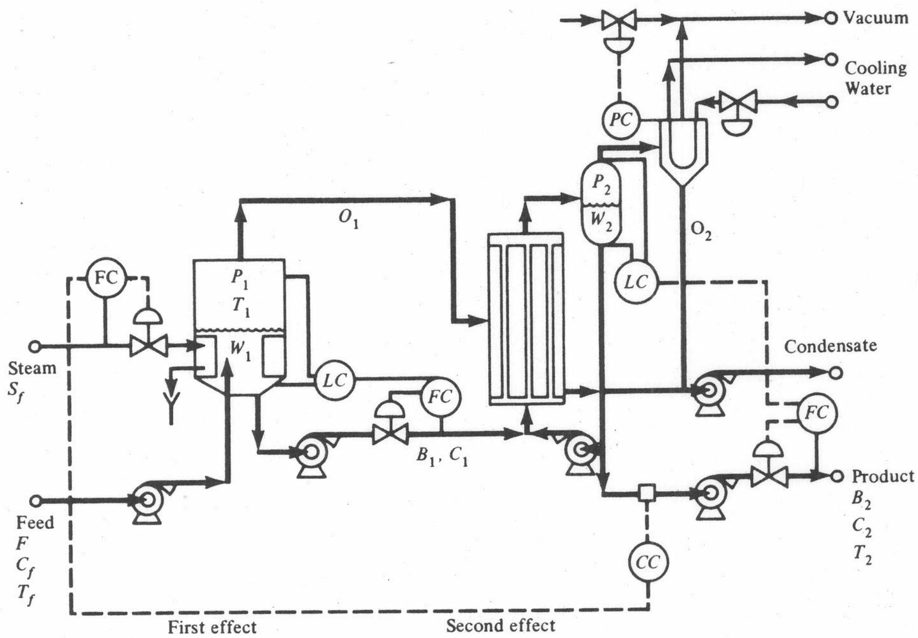

Figure 6.12 The pilot plant multiple-effect evaporator showing conventional single-loop controls. *(Reproduced from Proceedings 4th IFAC/IFIP Conference on Digital Computer Applications to Process Control,* 1974, *p.* 154, *by permission of Springer-Verlag.)*

implement the complicated dynamic noninteracting controller, then the steady-state noninteracting control scheme is preferred because it eliminates steady-state interactions for both set-point changes and disturbances.

6.3 THE CONTROL OF A MULTIPLE-EFFECT EVAPORATOR

As our second case study, we shall consider the computer control of the pilot plant multiple-effect evaporator shown in Fig. 6.12. A whole series of these case studies were carried out at the University of Alberta, Edmonton, Alberta, Canada by Professors Fisher and Seborg and their students through links to an IBM 1800 process control computer. In our discussion here we shall treat only a small part of their work and refer to their monograph [1] for the whole story. The goal of the present discussion is to illustrate the performance of several advanced process control algorithms when applied to this pilot plant process.

Modeling

The first step in this control study was to develop a simple yet reliable mathematical model of the process. The relevant variables and their steady-state values are given in Table 6.1. From Fig. 6.12 it is seen that the solution to be concentrated enters the first effect at feed rate F, solute concentration C_f, and

Table 6.1 Evaporator variables and steady-state values [1]

Variable	Feed	First Effect	Second Effect
B_1, B_2—bottoms flow rate (lb/min)	—	3.3	1.7
C_f, C_1, C_2—solute concentration (wt %)	3.2	4.85	9.64
F—feed flow rate (lb/min)	5.0	—	—
h_f, h_1—liquid enthalpy (Btu/lb)	1.62	194	—
S_f—steam flow rate (lb/min)	1.9	—	—
W_1, W_2—solute holdup (lb)	—	30	35
O_1, O_2—overhead vapor flow (lb/min)	—	1.7	1.6
T_f, T_1, T_2—temperature (°F)	190	225	160
P_1, P_2—pressure (psia)	—	<25	7.5

temperature T_f. For the present study the feed solution was triethylene glycol in water. Steam at rate S_f is injected into the first effect to vaporize the water, producing vapor stream O_1. The first-effect liquid effluent B_1 at concentration C_1 goes to the tube side of the second effect and is vaporized further under reduced pressure by condensation of the first-effect vapor stream on the shell side. The concentrated liquid B_2 from the second effect is the product at concentration C_2. The quantities W_1 and W_2 are the liquid holdups in each effect. A fifth-order nonlinear model of the evaporator was developed [1] under the following assumptions:

1. The heat capacitances of the steam chests, tube walls, etc., are all sufficiently small that they may be neglected.
2. The pressure controller on the second effect (see Fig. 6.12) is sufficiently powerful to hold the temperature in the second effect T_2 at steady state with negligible dynamic variations.
3. The solute concentration in the vapor leaving each effect of the evaporator is negligibly small compared with the amount of solute leaving in the liquid.

Under these conditions, total material, solute, and heat balances on the *first effect* may be written

$$\frac{dW_1}{dt} = F - B_1 - O_1 \tag{6.3.1}$$

$$W_1\frac{dC_1}{dt} = F(C_f - C_1) + O_1C_1 \tag{6.3.2}$$

$$W_1\frac{dh_1}{dt} = F(h_f - h_1) - O_1(H_{1v} - h_1) + Q_1 - L_1 \tag{6.3.3}$$

Similarly material balances on the *second effect* give

$$\frac{dW_2}{dt} = B_1 - B_2 - O_2 \tag{6.3.4}$$

$$W_2\frac{dC_2}{dt} = B_1(C_1 - C_2) + O_2C_2 \tag{6.3.5}$$

while a steady-state heat balance on the *second effect* yields

$$O_2\left(H_{2v} - h_2 + \frac{\partial h_2}{\partial C_2} C_2\right) = Q_2 - L_2 + B_1(h_1 - h_2) + \frac{\partial h_2}{\partial C_2} B_1(C_2 - C_1) \tag{6.3.6}$$

Here Q_1 and Q_2 are the heat inputs to each effect, given by

$$Q_1 = u_1 A_1 (T_s - T_1) = \lambda_s S_f \tag{6.3.7}$$

$$Q_2 = u_2 A_2 (T_1 - T_2) \tag{6.3.8}$$

The quantities L_1 and L_2 are the environmental heat losses from each effect; h_f, h_1, and h_2 are liquid enthalpies; H_{1v} and H_{2v} are the vapor enthalpies; and λ_s represents the heat of vaporization of the input steam at temperature T_s.

This set of equations constitutes a *fifth-order nonlinear model* of the process. By linearization of these equations around the steady state shown in Table 6.1, a *fifth-order linear model* may be obtained in the form

$$\dot{\mathbf{x}} = \mathbf{A}\mathbf{x} + \mathbf{B}\mathbf{u} + \mathbf{\Gamma}\mathbf{d} \tag{6.3.9}$$

$$\mathbf{y} = \mathbf{C}\mathbf{x} \tag{6.3.10}$$

where the state vector **x**, control vector **u**, disturbance vector **d**, and output vector **y** are

$$\mathbf{x} = \begin{bmatrix} W_1 \\ C_1 \\ h_1 \\ W_2 \\ C_2 \end{bmatrix} \qquad \mathbf{u} = \begin{bmatrix} S_f \\ B_1 \\ B_2 \end{bmatrix} \qquad \mathbf{d} = \begin{bmatrix} F \\ C_f \\ h_f \end{bmatrix} \qquad \mathbf{y} = \begin{bmatrix} W_1 \\ W_2 \\ C_2 \end{bmatrix} \tag{6.3.11}$$

while

$$\mathbf{A} = \begin{bmatrix} 0 & -0.00156 & -0.1711 & 0 & 0 \\ 0 & -0.1419 & 0.1711 & 0 & 0 \\ 0 & -0.00875 & -1.102 & 0 & 0 \\ 0 & -0.00128 & -0.1489 & 0 & 0.00013 \\ 0 & 0.0605 & 0.1489 & 0 & -0.0591 \end{bmatrix}$$

$$\mathbf{B} = \begin{bmatrix} 0 & -0.143 & 0 \\ 0 & 0 & 0 \\ 0.392 & 0 & 0 \\ 0 & 0.108 & -0.0592 \\ 0 & -0.0486 & 0 \end{bmatrix}$$

$$\mathbf{C} = \begin{bmatrix} 1 & 0 & 0 & 0 & 0 \\ 0 & 0 & 0 & 1 & 0 \\ 0 & 0 & 0 & 0 & 1 \end{bmatrix}$$

$$\mathbf{\Gamma} = \begin{bmatrix} 0.2174 & 0 & 0 \\ -0.074 & 0.1434 & 0 \\ -0.036 & 0 & 0.1814 \\ 0 & 0 & 0 \\ 0 & 0 & 0 \end{bmatrix} \tag{6.3.12}$$

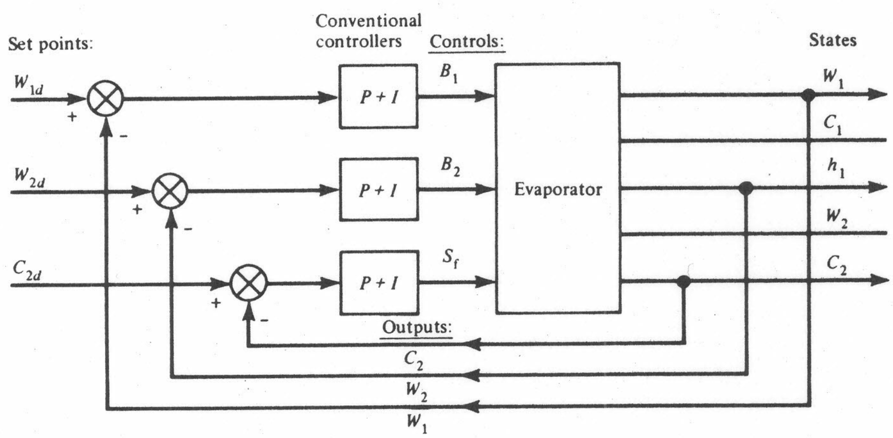

Figure 6.13 Block diagram for conventional control of the evaporator.

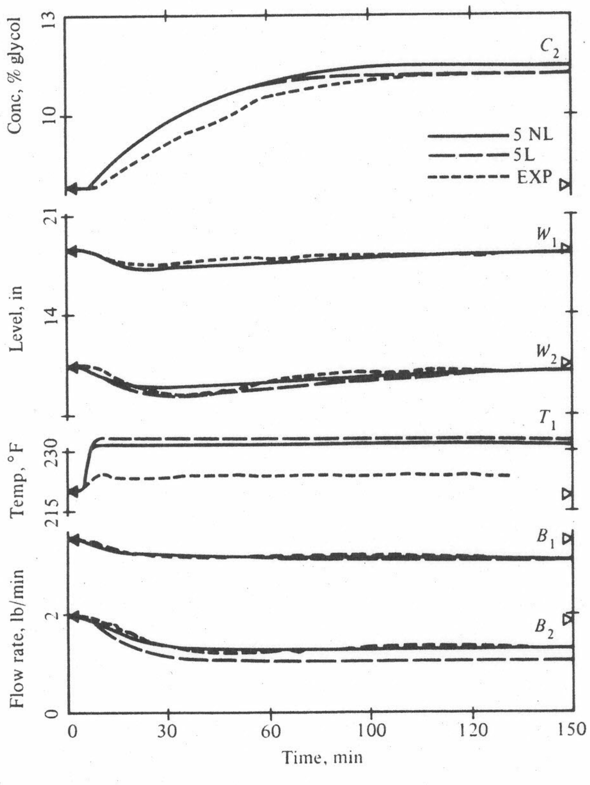

Figure 6.14 Comparison of fifth-order linear and nonlinear models with experimental data for the case of a 20% increase in stream feed rate. *(Reproduced with permission from I & EC Process Design Development* 11, 216 (1972). *Copyright by American Chemical Society.)*

The feedback relationship between controls **u** and outputs **y** under the conventional control scheme is shown in Fig. 6.13.

Figure 6.14 presents a typical comparison of both the nonlinear (5NL) and linear (5L) models with an experimental run under conventional control of W_1, W_2 for the case of a 20 percent increase in inlet steam flow-rate disturbance. Note that both models compare reasonably well with the experimental data except when predicting the temperature dynamics in the first effect. The model responds much more strongly than the experimental equipment, indicating that the thermal capacitance of the equipment itself should perhaps be included in Eq. (6.3.3).

Multivariable Control

Having developed a reliable linear model, we can now design multivariable control algorithms and compare these with the performance of the conventional single-loop control shown in Fig. 6.13. A large number of algorithms have been tested [1], but we shall only discuss the application of optimal multivariable feedback control algorithms here (see Chap. 3 to review the theory).

The standard optimal linear-quadratic multivariable controller design was modified to allow integral control action on the output variables. By defining a composite state vector $\hat{\mathbf{x}} = \begin{bmatrix} \mathbf{x} \\ \mathbf{z} \end{bmatrix}$, where

$$\dot{\mathbf{x}} = \mathbf{A}\mathbf{x} + \mathbf{B}\mathbf{u} + \mathbf{\Gamma}\mathbf{d} \tag{6.3.13}$$

$$\dot{\mathbf{z}} = \mathbf{y} - \mathbf{y}_d \tag{6.3.14}$$

$$\mathbf{y} = \mathbf{C}\mathbf{x} \tag{6.3.15}$$

and $\mathbf{y}_d$ is the set point of the output variables, one obtains the optimal feedback control law in the form (see Sec. 3.3)

$$\mathbf{u}(t) = -\mathbf{K}\hat{\mathbf{x}} = -\mathbf{K}_1\mathbf{x} - \mathbf{K}_2\mathbf{z} = -\mathbf{K}_1\mathbf{x} - \mathbf{K}_2\int_0^t (\mathbf{y} - \mathbf{y}_d)\,dt \tag{6.3.16}$$

thus yielding proportional and integral control. Recall that $\mathbf{K}_1$, $\mathbf{K}_2$ must be computed off-line from the solution of a Riccati equation. This controller, whose block diagram may be seen in Fig. 6.15, was implemented on the evaporator for the case where all five states were measured and optimal constant gains were used (corresponding to the infinite-time optimal control problem). Simulation results shown in Fig. 6.16 illustrate the superior performance of the optimal multivariable controller for both proportional and proportional plus integral action. An experimental comparison is seen in Fig. 6.17 and illustrates even more effectively the advantages of the optimal multivariable feedback control scheme over conventional control. Note that in both instances the conventional controller allowed significant upsets in the process dynamics, while the disturbances had almost no effect on the system under optimal multivariable control.

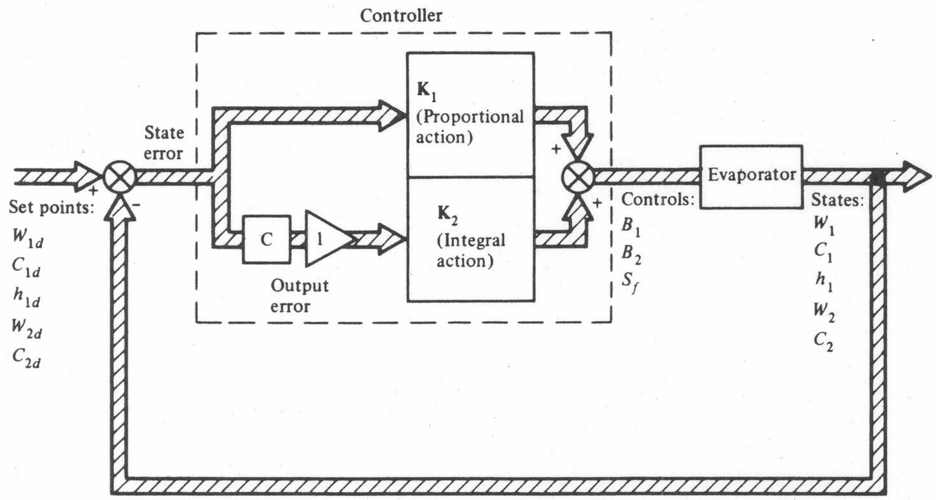

Figure 6.15 Deterministic optimal multvariable feedback control system having both proportional and integral action

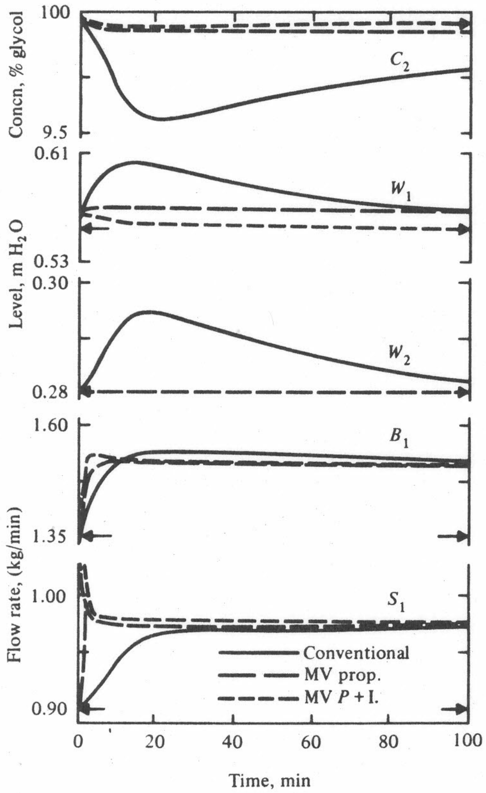

Figure 6.16 Simulation comparison of evaporator responses under optimal multivariable and conventional PI control. Disturbance: 10% increase in feed rate. *(Reproduced from Automatica* **8**, 247 (1972) *by permission of Pergamon Press Ltd.)*

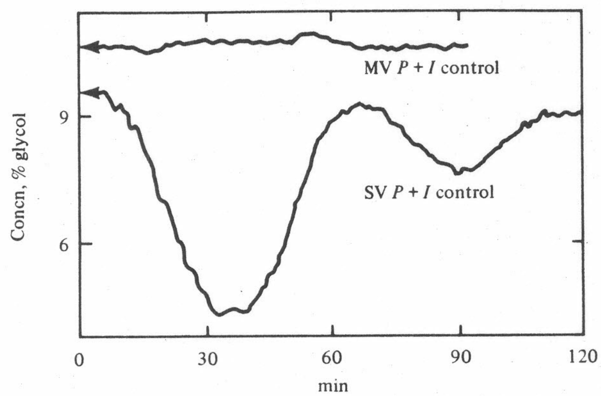

Figure 6.17 Comparison of experimental responses of evaporator product concentration using conventional PI controllers versus optimal multivariable control. Disturbance: 20% feed rate increase followed by decrease. *(Reproduced from Automatica* 8, 247 (1972) *by permission of Pergamon Press Ltd.)*

State Estimation and Stochastic Feedback Control

Fisher and Seborg [1] also carried out experimental evaluations of state-estimation and stochastic feedback control algorithms for the case when only W_1, W_2, and C_2 were available as outputs. A Luenberger observer and a Kalman filter (see Chap. 5) were implemented to estimate the state variables. Both of these were found to work well and give reliable estimates when properly tuned. These estimators were then coupled to the optimal multivariable feedback controller to form the stochastic feedback control system shown in Fig. 6.18.

When the observer was coupled to an optimal multivariable state feedback control scheme, the control system behavior may be seen in Fig. 6.19. These

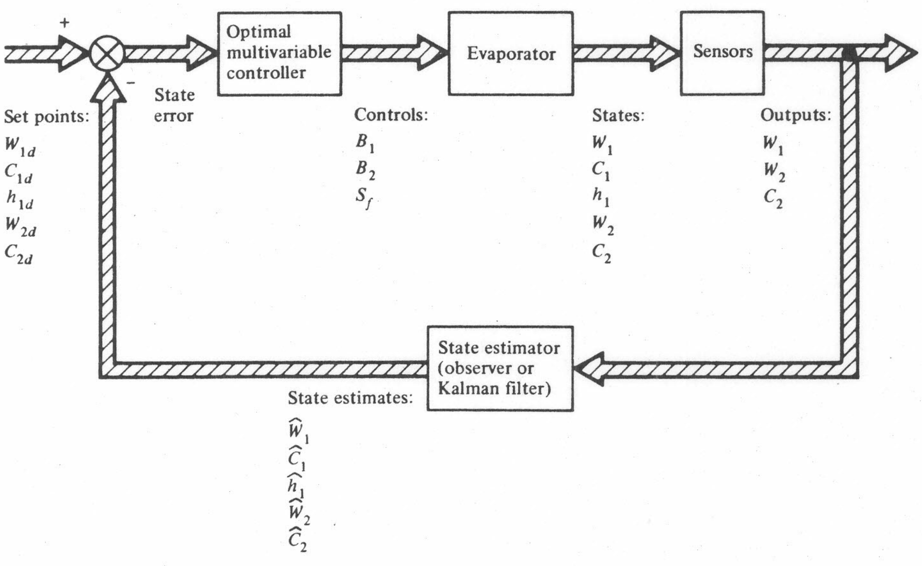

Figure 6.18 Stochastic optimal multivariable feedback control scheme utilizing an on-line state estimator.

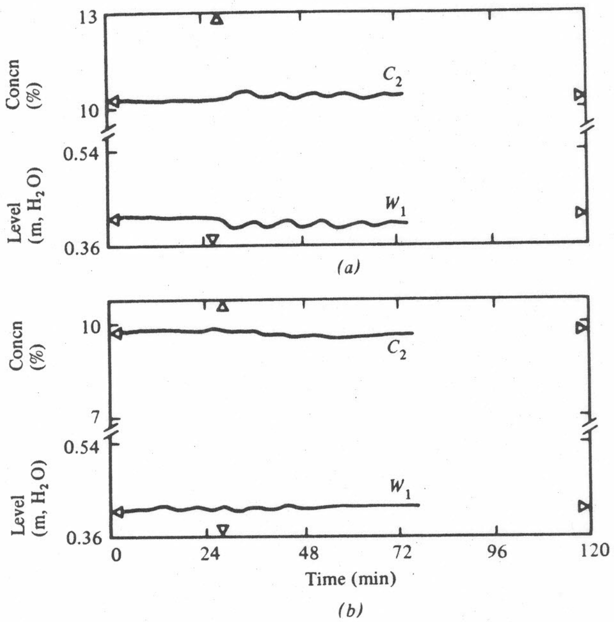

Figure 6.19 Optimal stochastic control system response with observer state estimates; disturbances: (*a*) single "unknown" 20% feed-rate decrease; (*b*) single "known" 30% decrease in feed solute concentration. *(Reproduced from Proceedings 4th IFAC/IFIP Conference on Digital Computer Applications to Process Control,* 1974, *p.* 154, *by permission of Springer-Verlag.)*

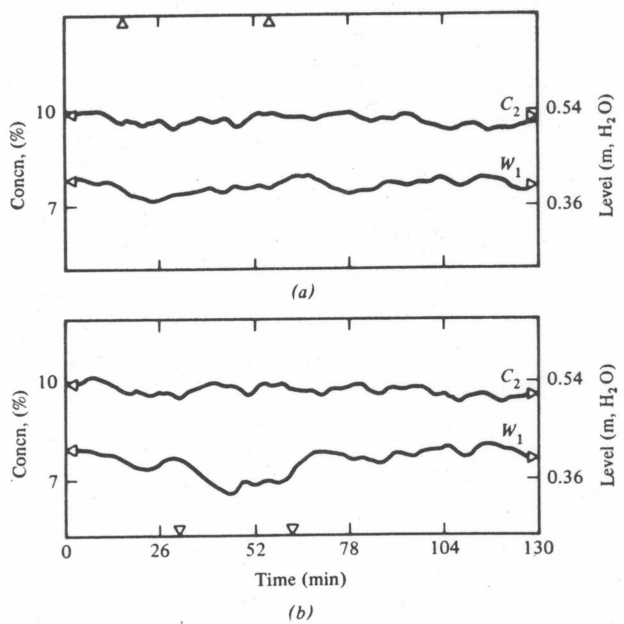

Figure 6.20 Optimal stochastic control system response with Kalman filter state estimates; disturbances: two 20% changes in feed rate at times denoted by ∇; (*a*) "known" disturbance, (*b*) "unknown" disturbance. *(Reproduced from Proceedings 4th IFAC/IFIP Conference on Digital Computer Applications to Process Control,* 1974, *p.* 154, *by permission of Springer-Verlag.)*

almost "bumpless" responses to rather large input disturbances are very impressive; however, the observer behavior was seen to deteriorate rapidly if the noise level of the data increased.

The Kalman filter, on the other hand, was found to be more robust in the face of noisy data. Some typical responses to feed-rate disturbances are shown in Fig. 6.20. Note that while the stochastic control system responds better to measured "known" disturbances, it also responds well to large "unknown" upsets.

Evaluation

The studies of Fisher and Seborg and their students [1] in applying advanced process algorithms to this pilot plant evaporator serve as a fine demonstration of computer control applied easily and profitably to an important chemical engineering process. Both the deterministic and stochastic multivariable feedback controllers performed well and proved to be a great improvement over the conventional control system.

6.4 A STRATEGY FOR STEEL MILL SOAKING PIT CONTROL

The soaking pit furnace is a major unit operation in the traditional steel mill. Large steel ingots which have been cast into molds and allowed to cool must be reheated in soaking pits to achieve a proper temperature distribution for rolling. Figure 6.21 shows the interior of a typical soaking pit. The ingots are placed in the furnace in a batchwise fashion, and some 6 to 12 h later they are removed for rolling in a rolling mill.

Unfortunately, the initial temperature distribution of the ingots is unknown, and the temperature distribution cannot be measured directly. Only furnace wall temperatures are routinely recorded, and these are augmented by sporadic optical pyrometric ingot surface temperature measurements. Thus it is difficult to determine how to control the furnace gas firing rate and to know when the ingots should be removed from the furnace. Too high a furnace firing rate will accelerate corrosion of the ingot surface (and can even cause surface melting), resulting in yield loss, while very low firing rates require excessive residence time in the furnace. Determining when the desired temperature distribution has been achieved (so that the ingots can be removed from the furnace) is even more of a problem. Removing ingots too soon results in poor rolling performance and requires the return of the ingot to the soaking pit for further heating. On the other hand, conservative, overlong heating cuts down the productivity of the process and increases production costs. In current steel mill practice, the furnace firing rate and ingot withdrawal time are based on certain "rules of thumb" and visual observations of an experienced operator, but steel industry figures indicate that this control scheme is not very reliable or effective.

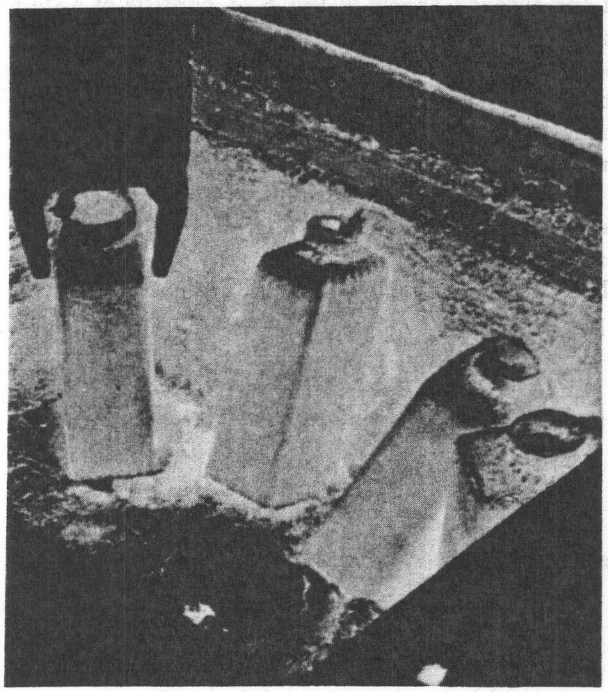

Figure 6.21 Ingots in a soaking pit furnace. *(Reproduced from "A Visit to STELCO" by permission of Steel Co. of Canada.)*

The present case study, described in more detail elsewhere [2–4], is devoted to testing the feasibility of an advanced process control scheme capable of solving these practical problems. Specifically, the control scheme must:

1. Estimate in real time the temperature distribution in the ingots residing in the soaking pit.
2. Provide a feedback control law for furnace firing rate.
3. Determine precisely when the ingots have achieved the desired temperature distribution and should be removed from the furnace.

Clearly specifications (1) and (3) call for on-line state estimation, while (2) requires feedback controller design based on these estimates. Because the ingots are distributed in nature, having a nearly cylindrical shape with both axial and radial temperature variations, our control strategy must involve distributed parameter state estimation and control algorithms such as those discussed in Chaps. 4 and 5. The equations to be solved for such algorithms are multidimensional partial differential equations, and the real-time computations could be substantial. Therefore, the principal aim of the feasibility study is to investigate the control system performance on a pilot plant process and to determine if the required computations can be readily performed in real time.

The pilot plant ingot and furnace, shown in Fig. 6.22, consists of a stainless steel cylindrical ingot in a three-zone electrical furnace. A hole was drilled through the center of the ingot, through which cooling water could be passed. This allowed rapid cooling of the ingot after a test so that a new run could begin. Although only ingot surface temperatures were made available to the control algorithm (to emulate optical pyrometry measurements in an actual soaking pit), the actual ingot temperature distribution was measured by 32 thermocouples placed at 8 axial positions z_i, $i = 1, 2, 3, \ldots, 8$, and 4 radial positions r_j, $j = 1, 2, 3$, and 4, as shown in Fig. 6.23.

The ingot was modeled assuming angular symmetry, negligible heat losses at each end, and constant physical parameters. Under these conditions, the ingot model takes the form

$$\frac{\partial T}{\partial t'} = \alpha\left(\frac{\partial^2 T}{\partial r'^2} + \frac{1}{r'}\frac{\partial T}{\partial r'} + \frac{\partial^2 T}{\partial z'^2}\right) \qquad 0 \le z' \le L$$

$$r_0' \le r \le R$$

$$t' > 0 \tag{6.4.1}$$

where $\alpha = k/\rho C_p$ is the thermal diffusivity and the boundary conditions are given as

$$\frac{\partial T}{\partial z'} = 0 \qquad \text{at } z' = 0 \tag{6.4.2}$$

$$\frac{\partial T}{\partial z'} = 0 \qquad \text{at } z' = L \tag{6.4.3}$$

$$k\frac{\partial T}{\partial r'} = h(T - T_w) \qquad \text{at } r' = r_0' \tag{6.4.4}$$

$$k\frac{\partial T}{\partial r'} = q'(z', t') \qquad \text{at } r' = R \tag{6.4.5}$$

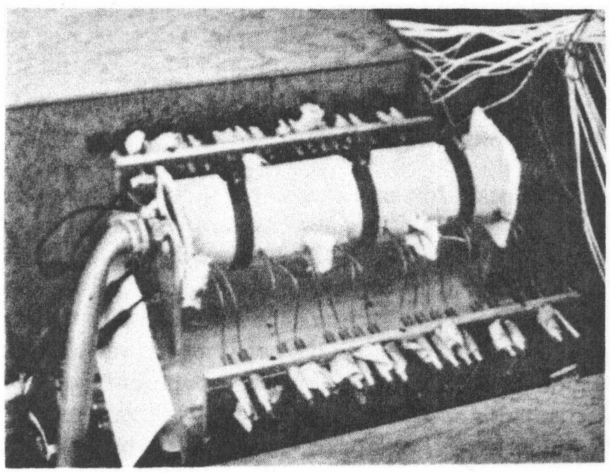

Figure 6.22 The experimental ingot and furnace system.

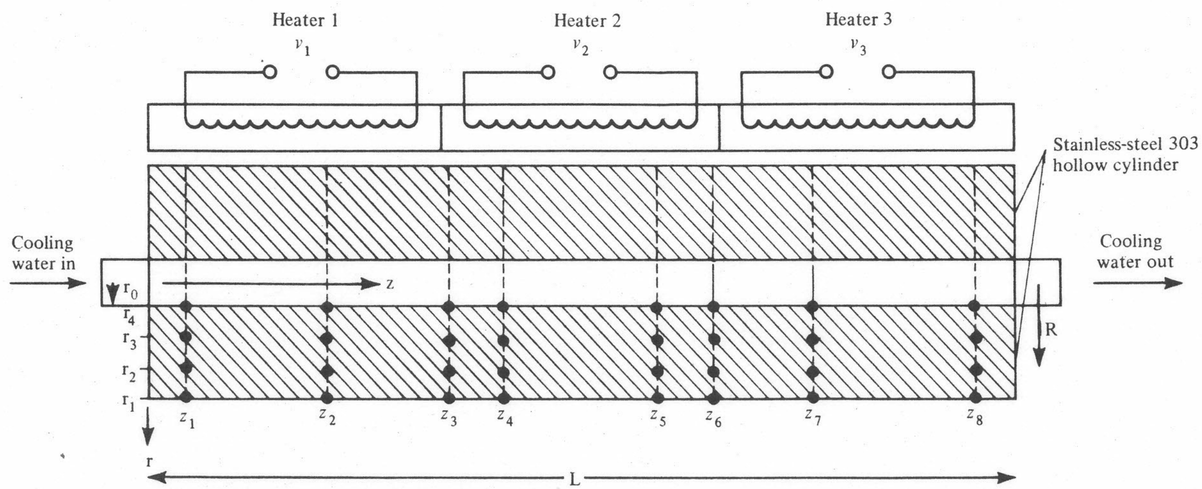

Figure 6.23 Axial cross section of the experimental apparatus.

Here k is the thermal conductivity, h is the experimentally determined overall heat transfer coefficient, T_w is the mean water temperature, and $q'(z', t')$ is the heat flux from the heaters at the outer surface into the cylinder. Let us define the following dimensionless quantities:

$$\theta = \frac{T - T_w}{T_w} \qquad z = \frac{z'}{l} \qquad r = \frac{r'}{R} \qquad r_0 = \frac{r'_0}{R}$$

$$t = \frac{\alpha t'}{R^2} \qquad \alpha' = \frac{R^2}{L^2} \qquad Bi = \frac{hR}{k}$$

$$q(z, t) = \frac{q'(z', t')R}{kT_w} = \mathbf{g}^T(z)\mathbf{v}(t) \tag{6.4.6}$$

where $g_i(z)$ is the spatial distribution of heat flux and $v_i(t)$ the heater power for the ith zone of the furnace. Then by inserting the heater input into the partial differential equations, in order to make the boundary conditions homogeneous, we obtain

$$\frac{\partial \theta}{\partial t} = \frac{\partial^2 \theta}{\partial r^2} + \frac{1}{r}\frac{\partial \theta}{\partial r} + \alpha' \frac{\partial^2 \theta}{\partial z^2} + \delta(r - 1)\mathbf{g}^T(z)\mathbf{v}(t) \tag{6.4.7}$$

$$\frac{\partial \theta}{\partial z} = 0 \qquad \text{at } z = 0 \qquad \text{and} \qquad z = 1 \tag{6.4.8}$$

$$\frac{\partial \theta}{\partial r} = Bi\theta \qquad \text{at } r = r_0 \tag{6.4.9}$$

$$\frac{\partial \theta}{\partial r} = 0 \qquad \text{at } r = 1 \tag{6.4.10}$$

The temperature measurements are given by

$$y_{ik}(t) = \theta(r_i, z_k, t) + \eta_{ik}(t) \qquad \begin{array}{l} i = 1, 2, 3, 4 \\ k = 1, 2, \ldots, 8 \end{array} \tag{6.4.11}$$

where η_{ik} represents the measurement error.

State Estimation

The first step in the control system synthesis is to develop the state estimation equations. By extending the linear distributed parameter state estimation results of Chap. 5 to two space dimensions, one obtains

$$\frac{\partial \hat{\theta}(r, z, t)}{\partial t} = \frac{\partial^2 \hat{\theta}(r, z, t)}{\partial r^2} + \frac{1}{r}\frac{\partial \hat{\theta}(r, z, t)}{\partial r} + \alpha' \frac{\partial^2 \hat{\theta}(r, z, t)}{\partial z^2} + \delta(r - 1)\mathbf{g}^T(z)\mathbf{v}(t)$$
$$+ \sum_{i=1}^{N_r} \sum_{j=1}^{N_r} \sum_{k=1}^{M_z} \sum_{l=1}^{M_z} P(r, r_i, z, z_k, t) Q_{ijkl}(t) \times \left[y_{jl}(t) - \hat{\theta}(r_j, z_l, t) \right] \tag{6.4.12}$$

which when solved with the boundary conditions of Eqs. (6.4.8) to (6.4.10) gives the estimated ingot temperature distribution, $\hat{\theta}(r, z, t)$.

The estimate covariance $P(r, s, z, u, t)$ is the solution of

$$\begin{aligned}\frac{\partial P(r, s, z, u, t)}{\partial t} &= \frac{\partial^2 P(r, s, z, u, t)}{\partial r^2} + \frac{1}{r}\frac{\partial P(r, s, z, u, t)}{\partial r} \\ &+ \frac{\partial^2 P(r, s, z, u, t)}{\partial s^2} + \frac{1}{s}\frac{\partial P(r, s, z, u, t)}{\partial s} + \alpha'\frac{\partial^2 P(r, s, z, u, t)}{\partial z^2} \\ &+ \alpha'\frac{\partial^2 P(r, s, z, u, t)}{\partial u^2} - \sum_{i=1}^{N_r}\sum_{j=1}^{N_r}\sum_{k=1}^{M_z}\sum_{l=1}^{M_z} P(r, r_i, z, z_k, t) Q_{ijkl}(t) \\ &\times P(r_j, s, z_l, u, t) + R^+(r, s, z, u, t) \qquad \begin{array}{l} r_0 \le r \le 1 \\ 0 \le z \le 1 \\ 0 \le t \le t_f \end{array}\end{aligned} \tag{6.4.13}$$

with the boundary conditions

$$\frac{\partial P(r, s, z, u, t)}{\partial r} - BiP(r, s, z, u, t) + R_0^{-1}(t)\delta(s - r_0) = 0 \qquad \text{at } r = r_0 \tag{6.4.14}$$

$$\frac{\partial P(r, s, z, u, t)}{\partial r} - R_1^{-1}(t)\delta(s - 1) = 0 \qquad \text{at } r = 1 \tag{6.4.15}$$

$$\frac{\partial P(r, s, z, u, t)}{\partial z} + \alpha' R_2^{-1}(t)\delta(u) = 0 \qquad \text{at } z = 0 \tag{6.4.16}$$

$$\frac{\partial P(r, s, z, u, t)}{\partial z} - \alpha' R_3^{-1}(t)\delta(u - 1) = 0 \qquad \text{at } z = 1 \tag{6.4.17}$$

A similar set of boundary conditions holds for $s = r_0$, $s = 1$ and $u = 0$, $u = 1$.

Because the system is linear, both the filter and covariance equations may be solved by a modal decomposition of the form

$$\hat{\theta}(r, z, t) = \sum_{n=1}^{N}\sum_{m=1}^{M} \hat{a}_{nm}(t)\phi_n(r)\psi_m(z) \tag{6.4.18}$$

$$P(r, s, z, u, t) = \sum_{n=1}^{N_c}\sum_{k'=1}^{N_c}\sum_{m=1}^{M_c}\sum_{p=1}^{M_c} p_{nk'mp}(t)\phi_n(r)\phi_{k'}(s)\psi_m(z)\psi_p(u) \tag{6.4.19}$$

where N, M and N_c, M_c represent the number of terms in the eigenfunction expansion necessary for an adequate representation of the filter and covariance, respectively. Here the $\phi_n(r)$, $\psi_m(z)$ are eigenfunctions of the system [1–3] given by

$$\phi_n(r) = A_n\left[J_0(\sqrt{\mu_n}\,r) - \frac{J_1(\sqrt{\mu_n})Y_0(\sqrt{\mu_n}\,r)}{Y_1(\sqrt{\mu_n})}\right] \tag{6.4.20}$$

$$\psi_m(z) = \begin{cases} 1 & m = 1 \\ \sqrt{2}\cos(m-1)\pi z & m > 1 \end{cases} \tag{6.4.21}$$

The quantities A_n, μ_n may be determined from the solution to certain transcendental equations [2–4]. The time-dependent coefficients $\hat{a}_{nm}(t)$ and $p_{nk'mp}(t)$ are the solutions of

$$\begin{aligned}\frac{d\hat{a}_{nm}(t)}{dt} = -\lambda_{nm}\hat{a}_{nm}(t) + \sum_{k'=1}^{N_c}\sum_{p=1}^{M_c}\sum_{i=1}^{N_r}\sum_{j=1}^{N_r}\sum_{k=1}^{M_z}\sum_{l=1}^{M_z} p_{nk'mp}(t) \\ \times \phi_{k'}(r_i)\psi_p(z_k)Q_{ijkl}(t)\left[y_{jl} - \sum_{n'=1}^{N}\sum_{m'=1}^{M}\hat{a}_{n'm'}(t)\phi_{n'}(r_j)\psi_{m'}(z_l)\right] + u^*_{nm}(t)\end{aligned} \tag{6.4.22}$$

$$\begin{aligned}\frac{dp_{nk'mp}(t)}{dt} = -\gamma_{nk'mp}p_{nk'mp}(t) - \sum_{n'=1}^{N_c}\sum_{l'=1}^{N_c}\sum_{m'=1}^{M_c}\sum_{p'=1}^{M_c}\sum_{i=1}^{N_r}\sum_{j=1}^{N_r}\sum_{k=1}^{M_z}\sum_{l=1}^{M_z} \\ \times p_{nl'mp'}(t)\phi_{l'}(r_i)\psi_{p'}(z_k)Q_{ijkl}(t)\phi_{n'}(r_j)\psi_{m'}(z_l)p_{n'k'm'p}(t) \\ + r_{nk'mp}(t) + \sum_{i=0}^{3} r_{i_{nk'mp}}(t)\end{aligned} \tag{6.4.23}$$

where

$$\lambda_{nm} = \mu_n + \alpha'[(m-1)\pi]^2 \tag{6.4.24}$$

$$u^*_{nm}(t) = \int_0^1 \phi_n(1)\psi_m(z)\mathbf{g}^T(z)\mathbf{v}(t)\,dz \tag{6.4.25}$$

The covariance equations (6.4.23) may be solved off-line, so that only the state estimator equations (6.4.22) must be solved in real time. The experimental testing of this state estimator and subsequent controller designs was accomplished using the communications and computing scheme shown in Fig. 6.24. Temperature measurements were transmitted to the computer, which carried out the estimation and control calculations necessary to determine adjustments to be made in the heater power to the three zones of the furnace.

Optimal Stochastic Feedback Control

In order to control the furnace heat input, a distributed linear-quadratic optimal stochastic feedback controller was developed and tested.* For this problem, the

* See Chaps. 4 and 5 to review the necessary theory.

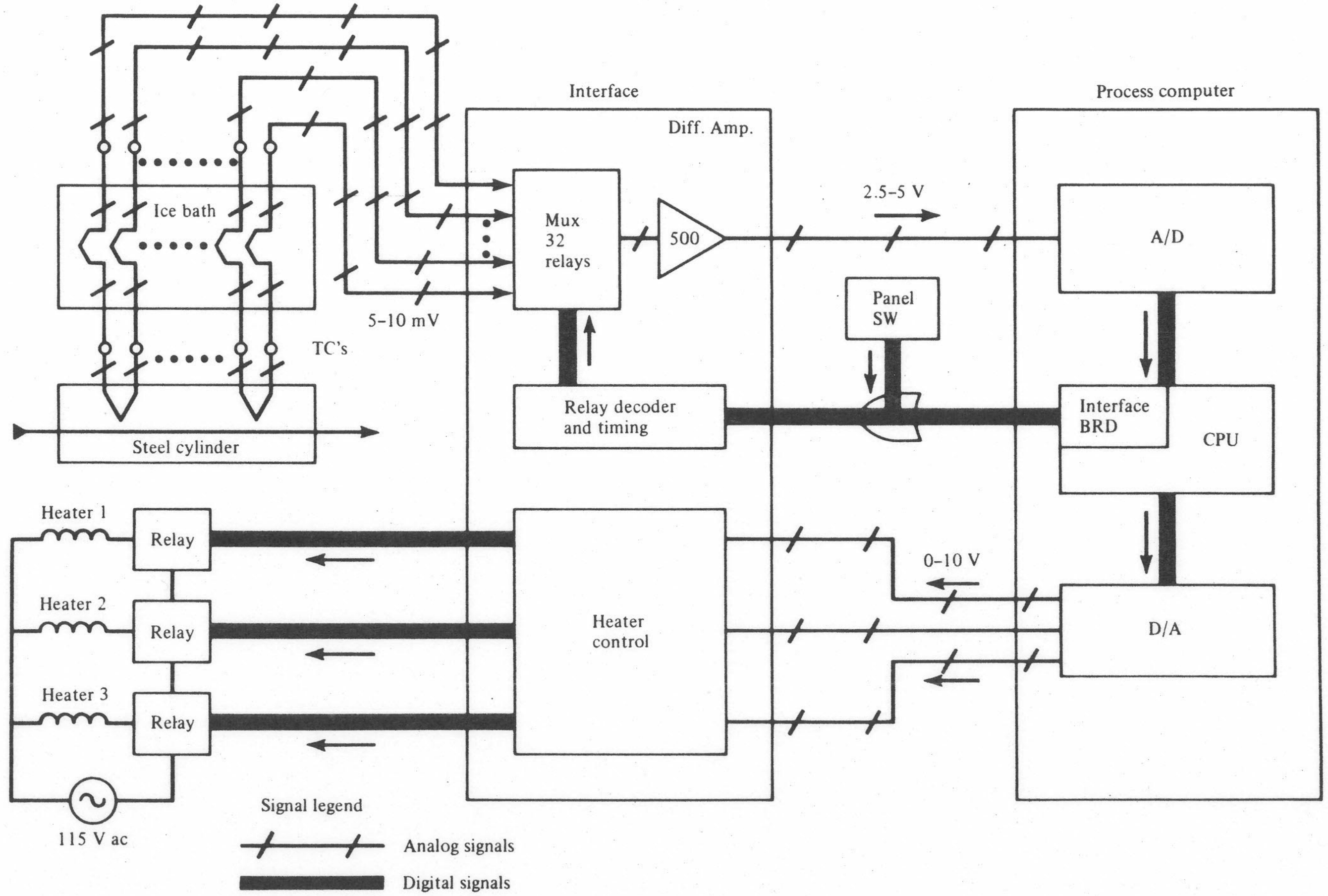

Figure 6.24 Communications for on-line testing of the ingot-furnace system.

control law takes the form [2–4]

$$\mathbf{v}(t) = \mathbf{v}^*(t) + \boldsymbol{\Gamma}_u^{-1} \int_0^1 \int_0^1 \int_{r_0}^1 \int_{r_0}^1 R_c(r, r', z, z', t)$$
$$\times \left[\theta_d(r', z', t) - \bar{\hat{\theta}}(r', z', t)\right] \mathbf{g}(z)\delta(r-1)\, dr\, dr'\, dz\, dz' \qquad (6.4.26)$$

where θ_d is the desired temperature distribution set point, $\mathbf{v}^*(t)$ is the furnace heat flux which holds θ at θ_d, and R_c is found from the solution of

$$\frac{\partial R_c}{\partial t} = -\frac{\partial^2 R_c}{\partial r^2} + \frac{\partial}{\partial r}\left(\frac{1}{r} R_c\right) - \frac{\partial^2 R_c}{\partial r'^2} + \frac{\partial}{\partial r'}\left(\frac{1}{r'} R_c\right)$$
$$- \alpha'\left(\frac{\partial^2 R_c}{\partial z^2} + \frac{\partial^2 R_c}{\partial z'^2}\right) + \gamma_d(r, r', z, z', t)$$
$$- \int_0^1 \int_0^1 \int_{r_0}^1 \int_{r_0}^1 R_c(r, \rho, z, \xi, t)\delta(\rho - 1)\mathbf{g}^T(\xi)\boldsymbol{\Gamma}_u^{-1}\delta(\rho' - 1)\mathbf{g}(\xi')$$
$$\times R_c(\rho', r', \xi', z', t)\, d\rho\, d\rho'\, d\xi\, d\xi' \qquad (6.4.27)$$

with boundary conditions being the adjoint of those given by Eqs. (6.4.14) to (6.4.17). Here $\boldsymbol{\Gamma}_u$ and γ_d are controller weighting parameters. The quantity R_c may be expanded in terms of the adjoint eigenfunctions to yield

$$R_c(r, r', z, z', t) = \sum_{n=1}^{N_R} \sum_{m=1}^{M_R} \sum_{k'=1}^{N_R} \sum_{p=1}^{M_R} r^c_{nk'mp}(t) r r' \phi_n(r)\phi_{k'}(r')\psi_m(z)\psi_p(z') \qquad (6.4.28)$$

and $r^c_{nk'mp}(t)$ is the solution of

$$\frac{dr^c_{nk'mp}}{dt} = \gamma_{nk'mp} r^c_{nk'mp}(t) - \gamma^d_{nk'mp}$$
$$+ \sum_{n'=1}^{N_R} \sum_{m'=1}^{N_R} \sum_{l'=1}^{M_R} \sum_{p'=1}^{M_R} r^c_{n'k'm'p'}(t)\mathbf{b}^T_{n'm'}\boldsymbol{\Gamma}_u^{-1}\mathbf{b}_{l'p'} r^c_{nl'mp'}(t) \qquad (6.4.29)$$

where

$$\mathbf{b}_{nm} = \int_0^1 \int_{r_0}^1 r\phi_n(r)\psi_m(z)\mathbf{g}(z)\delta(r-1)\, dr\, dz \qquad (6.4.30)$$

and

$$\gamma^d_{nk'mp}(t) = \int_0^1 \int_0^1 \int_{r_0}^1 \int_{r_0}^1 \gamma_d(r, r', z, z', t)\phi_n(r)\phi_{k'}(r')\psi_m(z)\psi_p(z')\, dr\, dr'\, dz\, dz' \qquad (6.4.31)$$

Finally, the feedback control law, Eq. (6.4.26), may be put in the simpler form

$$\mathbf{v}(t) = \mathbf{v}^*(t) + \boldsymbol{\Gamma}_u^{-1} \sum_{n=1}^{N_R} \sum_{k'=1}^{N_R} \sum_{m=1}^{M_R} \sum_{p=1}^{M_R} r^c_{nk'mp}(t)\mathbf{b}_{nm}\left(a^d_{k'p}(t) - \hat{a}_{k'p}(t)\right) \qquad (6.4.32)$$

where $a^d_{k'p}(t)$ is the eigencoefficient of the temperature set point $\theta_d(r', z', t)$ given by the orthogonality relation

$$a^d_{k'p}(t) = \int_0^1 \int_{r_0}^1 \phi_{k'}(r')\psi_p(z')\theta_d(r', z', t)\, dr'\, dz' \tag{6.4.33}$$

and $\hat{a}_{k'p}(t)$ is the eigencoefficient of the state estimator determined previously. The Riccati equation (6.4.29) may be solved off-line, so that only the optimal feedback control law, Eq. (6.4.32), need be calculated in real time.

Case 1 As a first test of the state estimator alone, all eight ingot surface temperatures were provided to the estimator. These measurements were corrupted with Gaussian random errors having zero mean and $\sigma = 10°C$ and taken from a random number generator. The initial conditions, seen in Fig. 6.25, show the estimated temperature distribution as uniform and some 10 to 20°C below the actual distribution. For this case two radial and five axial eigenfunctions were used, so that the *off-line* solution of the covariance equations (6.4.23) consisted of integrating 45 differential equations. By contrast, the on-line solution of the estimator equations (6.4.22) required solving only 10 differential equations in real time. The results after 120 s show the filter tracking the actual temperature distribution quite well (Fig. 6.26), and it continues to provide good estimates as the ingot is heated further (Fig. 6.27).

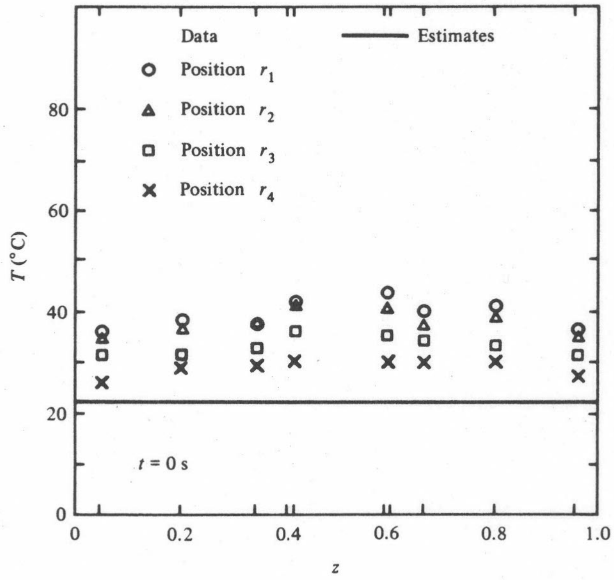

Figure 6.25 Initial estimates and data, Case 1.

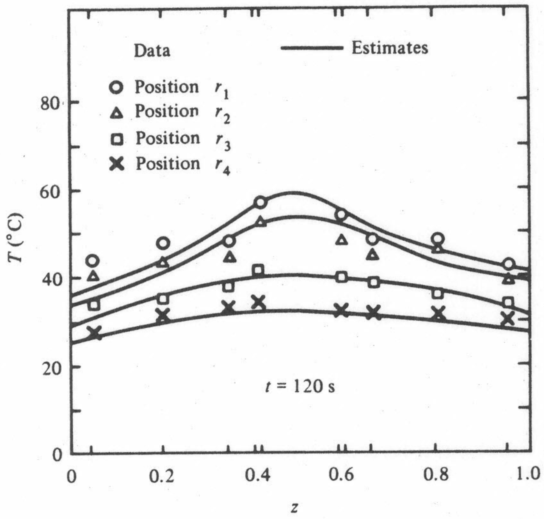

Figure 6.26 Filter estimates and data after 120 s, Case 1.

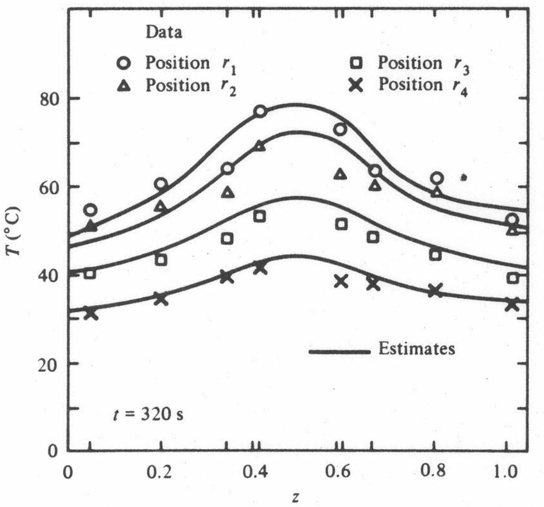

Figure 6.27 Filter estimates and data after 320 s, Case 1.

Case 2 As a test of what might prove to be the final control system design, only a single ingot surface thermocouple $\theta(r_1, z_3, t)$ was provided for the state estimator (see Fig. 6.28). The state estimates were then compared with the set-point value and the error fed to an optimal feedback controller which adjusts the furnace heat inputs. As in Case 1, zero-mean Gaussian measurement errors with $\sigma = 10°C$ were added to the actual temperature measurement to simulate very noisy steel mill conditions. The performance of the control scheme may be seen in Figs. 6.29 to 6.31. As shown in Fig. 6.29, the estimator initial condition is some 20 to 25°C below the actual ingot temperature distribution, and the temperature distribution set point is much different from the initial values. After 40 s (Fig. 6.30) the estimator is beginning to track the true temperature distribution, and by 320 s (Fig. 6.31) both the estimated and actual temperature distributions approximate the set point quite well.

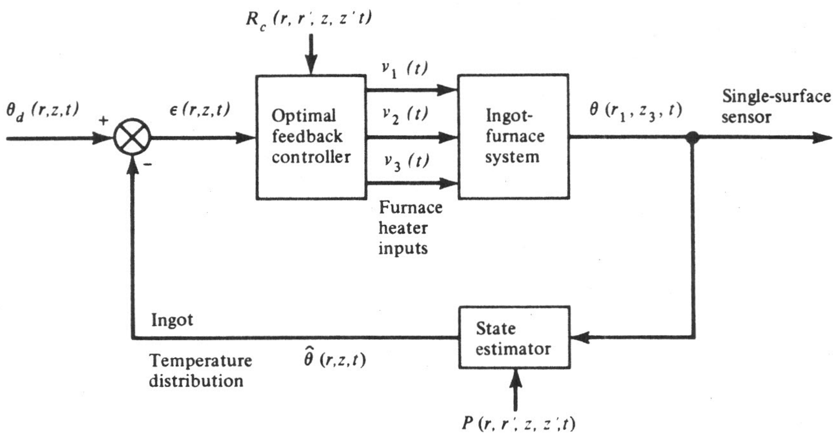

Figure 6.28 Estimator-controller for the soaking pit requiring only one surface temperature sensor.

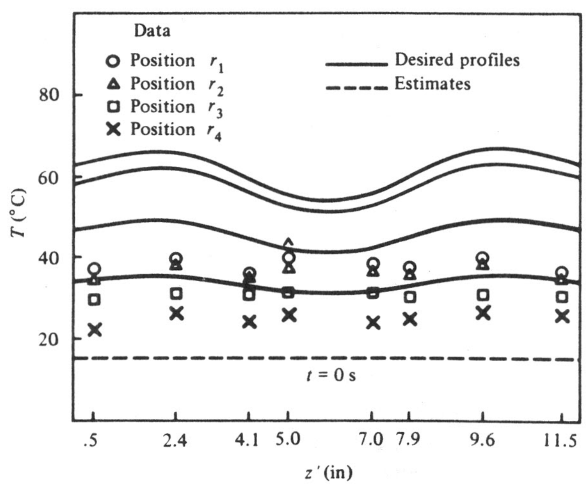

Figure 6.29 Stochastic feedback controller with one sensor.

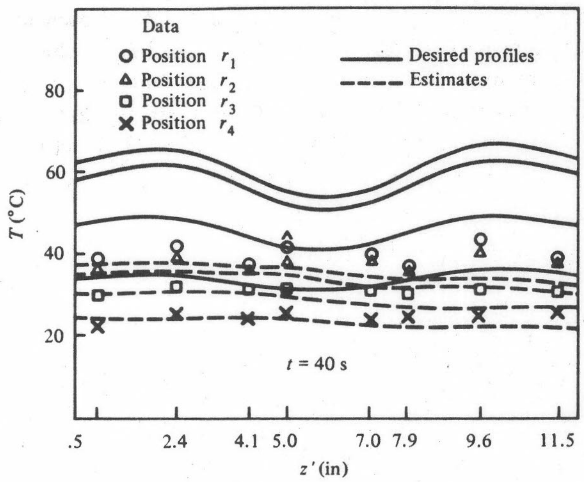

Figure 6.30 Stochastic feedback controller with one sensor; system evolution at 40 s.

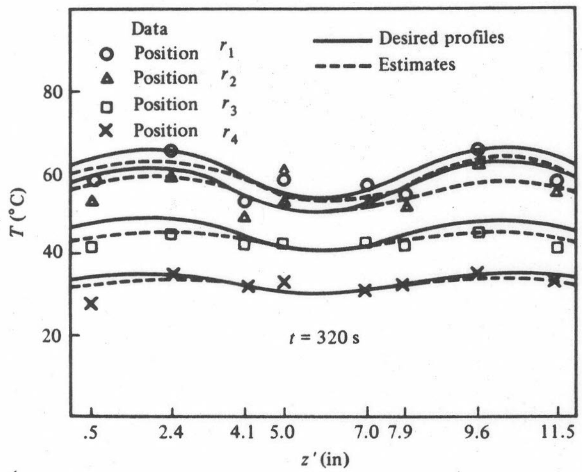

Figure 6.31 Stochastic feedback controller with one sensor; system evolution at 320 s.

Evaluation

The performance of the combined estimator/controller system, shown in Fig. 6.28, seems outstanding, allowing good control system performance when only one noisy temperature sensor is provided to the control system. The on-line computational requirements were less than 25 percent of real time for this pilot plant soaking pit having a principal time constant of about 5 min. This means that for industrial-scale soaking pits with time constants of 5 h or more, these computational requirements amount to less than $\frac{1}{2}$ percent of real time. This suggests that a hundred or more soaking pits could be controlled by the same computer in an actual steel mill.

This case study provides an important philosophical lesson for the control system designer. One should not be disheartened by control system designs involving formidable partial differential equations in many space dimensions [such as Eqs. (6.4.12) to (6.4.17), (6.4.26), and (6.4.27)] because it is often possible, as was done here, to reduce these to manageable proportions through judicious use of engineering judgment and numerical analysis. The effort is usually worthwhile because the resulting control system performance can be quite impressive, as was the case here.

6.5 CONTROL OF METALLURGICAL CASTING OPERATIONS

Another type of steel mill unit operation of great importance is casting. This process is carried out both batchwise in molds and continuously in continuous casting machines. Often it is important to control these casting processes so as to prevent excessive thermal stresses which lead to crack formation, and to prevent "breakout" of molten steel in the continuous process. The goal of the present case study is to develop and test the feasibility of a control system for a continuous casting machine.

The continuous casting of steel is an increasingly important part of modern steelmaking because it is a much more efficient route to steel slabs and billets than the conventional ingot casting-reheating-slab rolling operation. The process, sketched in Fig. 6.32, involves pouring molten steel at the top of a water-cooled mold and continuously drawing out a thin-walled steel slab or billet at the bottom. If the solid steel crust is too thin when it leaves the mold, either because of some process upset or because the withdrawal rates are too high, the molten steel core will "break out" and the casting machine must be shut down. By employing a distributed parameter filter to estimate the steel shell thickness in real time, one could operate at high average withdrawal rates while detecting potential breakouts before they occur and taking appropriate control action.

Although a very detailed model for this process has been developed [5, 6], the following simple model has been found to be adequate for the mold region. This idealized picture, illustrated in Fig. 6.33, approximates the two-phase "mushy" zone shown in Fig. 6.32 by an interface.

Assume that:

1. The solid at temperature $T_S(r', z', t')$ is moving downward at speed u_c while the liquid region is well mixed.
2. The physical properties are constant.
3. There is heat transfer to the mold wall with heat transfer coefficient h.

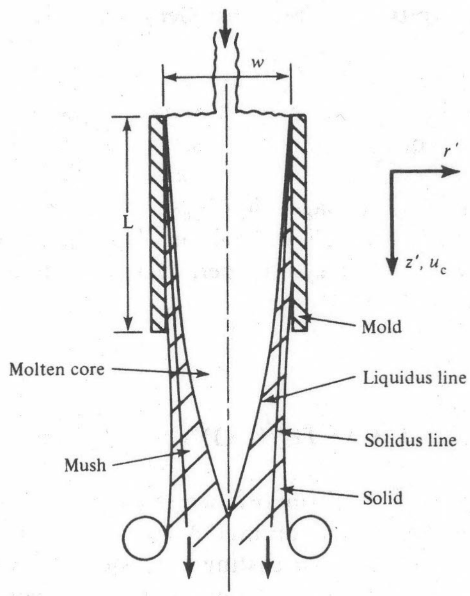

Figure 6.32 The continuous casting process.

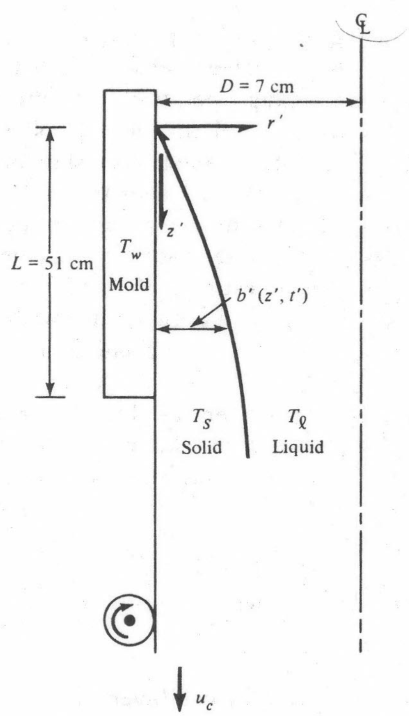

Figure 6.33 The mold region of a continuous casting operation.

4. There is heat transfer from the molten liquid to the solid at $r' = b'$ with heat transfer coefficient h_l and latent heat of solidification, $\mathcal{L}$.
5. The solid-liquid interface is at the solidus temperature, T_{sol}.

Then the modeling equations take the form

$$\frac{\partial T_S(r', z', t')}{\partial t'} + u_c \frac{\partial T_S(r', z', t')}{\partial z'} = \alpha_s \frac{\partial^2 T_S(r', z', t')}{\partial r'^2} \tag{6.5.1}$$

with boundary conditions

$$z'=0 \qquad T_S(r', 0, t) = T_l(t') \tag{6.5.2}$$

$$r'=0 \qquad k_s \frac{\partial T_S}{\partial t'} = h[T_S(0, z', t') - T_w] \tag{6.5.3}$$

$$r'=b'(z', t') \qquad T_S = T_{sol} \tag{6.5.4}$$

and moving boundary condition

$$\frac{\partial b'(z', t')}{\partial t'} = \frac{k_s}{\mathcal{L}\rho_s} \frac{\partial T_S}{\partial r'}\bigg|_{r'=b'(z', t')} + \frac{h_l}{\mathcal{L}\rho_l}[T_S(b', z', t) - T_l(t')] \tag{6.5.5}$$

Equation (6.5.5) represents a heat balance over the moving interface and states that the net heat flux at $r' = b'$ is balanced by solidification.

It is possible to eliminate the variable z' from the model by noting that the vertical flow in the mold is along the characteristic lines

$$\frac{dz'}{dt'} = u_c \qquad z'(0) = z_0' \tag{6.5.6}$$

Thus the solution along these characteristic lines may be determined from

$$\frac{\partial T_S(r', t')}{\partial t'} = \alpha_S \frac{\partial^2 T_S(r', t')}{\partial r'^2} \qquad 0 < r' < b'(t') \tag{6.5.7}$$

$$r'=0 \qquad k_S \frac{\partial T_S}{\partial r'} = h[T_S(0, t') - T_w] \tag{6.5.8}$$

$$r'=b'(t') \qquad T_S = T_{sol} \tag{6.5.9}$$

$$t'=0 \qquad T_S(r', 0) = T_l(t') \tag{6.5.10}$$

$$\frac{db'(t')}{dt'} = \frac{k_S}{\mathcal{L}\rho_S} \frac{\partial T_S}{\partial r'}\bigg|_{r'=b'(t')} + \frac{h_l}{\mathcal{L}\rho_l}[T_S(b', t') - T_l(t')] \tag{6.5.11}$$

These equations are nonlinear due to the moving boundary; thus we shall make some transformations which will convert the equations to a *fixed-boundary* *problem*. Let us define the variables

$$\theta_S = \frac{T_S - T_{sol}}{T_{sol}} \qquad r = \frac{r'}{b'(t')} \qquad b(t') = \frac{b'(t')}{D}$$

$$\theta_w = \frac{T_w - T_{sol}}{T_{sol}} \qquad H = \frac{hD}{k_S} \qquad \eta = \frac{k_S T_{sol}}{\rho_S \mathfrak{L} \alpha_S}$$

$$\theta_l = \frac{T_l - T_{sol}}{T_{sol}} \qquad K = \frac{h_l D}{\alpha_S \mathfrak{L} \rho_l} T_{sol} \qquad t = \int_0^{t'} \frac{\alpha_S}{b'(t'')^2}\, dt'' \tag{6.5.12}$$

By substituting Eq. (6.5.12) into Eqs. (6.5.7) to (6.5.11) and making the boundary conditions homogeneous through the use of a Dirac delta function, the model becomes

$$\frac{\partial \theta_S(r,t)}{\partial t} = \frac{\partial^2 \theta_S(r,t)}{\partial r^2} + r\frac{d \ln b(t)}{dt}\frac{\partial \theta_S(r,t)}{\partial r}$$
$$- b(t)H(\theta_S(0,t) - \theta_w)\delta(r) \qquad 0 < r < 1 \tag{6.5.13}$$

$$\frac{d \ln b(t)}{dt} = \eta \frac{\partial \theta_S}{\partial r}\Big|_{r=1} - Kb(t)\theta_l(t) \tag{6.5.14}$$

$$r = 0 \qquad \frac{\partial \theta_S}{\partial r} = 0 \tag{6.5.15}$$

$$r = 1 \qquad \theta_S = 0 \tag{6.5.16}$$

In dimensionless form, the solid surface temperature measurements (obtained from thermocouples placed in the mold surface) take the form

$$y(t) = \theta_S(0,t) + \epsilon(t) \tag{6.5.17}$$

where $\epsilon(t)$ is a random measurement error.

In order to test the validity of the model, simulations were carried out for the conditions shown in Table 6.2 and compared with experimental data for the

Table 6.2

Property values used in the computation [4]

$T_{sol} = 1495°C$
$T_{liq} = 1523°C$
$C_{p_S} = C_{p_l} = 0.16$ cal/(g)(°C)
$k_S = k_l = 7.02 \times 10^{-3}$ cal/(cm)(s)(°C)
$T_l = 1525°C$
$h_l = 0.01355$ cal/(cm^2)(s)(°C)
$u_c = 2.34$ cm/s
$T_c = 21°C$
$h = 0.044\left(\frac{1 - 0.98z'}{100}\right)$ cal/(cm^2)(s)(°C) (z' is cm)
$\rho_S = \rho_l = 7.4$ g/cm^3
$D = 7$ cm

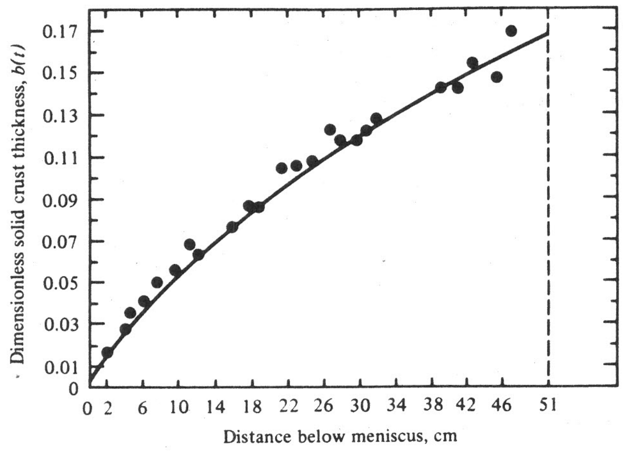

Figure 6.34 A comparison of the model predictions with experimental data.

same operating conditions. The model predictions for solid crust thickness versus time (or axial position), shown in Fig. 6.34, are in excellent agreement with the data; thus it appears that the model is representative of actual experimental operations, and we may proceed in confidence with the state estimation study.

State Estimation

The crux of the control scheme for the continuous caster is a state estimation algorithm which receives temperature data from thermocouples in the mold wall [Eq. (6.5.17)] and provides estimates of the solid crust thickness $b(t)$ as well as the solid temperature distribution $\theta_S(r, t)$. The optimal least squares state estimation equations [5, 6] take the form

$$\frac{\partial \hat{\theta}_S}{\partial t} = \frac{\partial^2 \hat{\theta}_S}{\partial r^2} + r\frac{d \ln \hat{b}(t)}{dt}\frac{\partial \hat{\theta}_S}{\partial r} - b(t)H\big(\hat{\theta}_S(0, t) - \theta_w\big)\delta(r) + P^{uu}(r, 0, t)Q(t)\big(y - \hat{\theta}_S(0, t)\big) \tag{6.5.18}$$

$$\frac{d\hat{b}(t)}{dt} = \eta\hat{b}\frac{\partial \theta_S}{\partial r}\Big|_{r=1} - K\hat{b}^2\theta_l(t) + P^{ub}(0, t)Q(t)\big(y - \hat{\theta}_S(0, t)\big) \tag{6.5.19}$$

$$\hat{\theta}_S(1, t) = 0 \tag{6.5.20}$$

$$\frac{\partial \hat{\theta}_S(0, t)}{\partial r} = 0 \tag{6.5.21}$$

where $P^{uu}(r, s, t)$, $P^{ub}(r, t)$, and $P^{bb}(t)$ are the relevant differential sensitivities (i.e., nonlinear "covariances"), determined by

$$P_t^{uu}(r, s, t) = P_{rr}^{uu} + P_{ss}^{uu} - P^{bu}(s, t)\frac{r}{\hat{b}^2}\frac{d\hat{b}}{dt}\frac{\partial\hat{\theta}_S}{\partial r} + H(\hat{\theta}_S(0, t) - \theta_w)\delta(r)$$

$$- P^{ub}(r, t)\frac{s}{\hat{b}^2}\frac{d\hat{b}}{dt}\frac{\partial\hat{\theta}_S}{\partial s} + H(\hat{\theta}_S(0, t) - \theta_w)\delta(s)$$

$$- P^{uu}(r, 0, t)Q(t)P^{uu}(0, s, t)$$

$$+ P_s^{uu}(r, s, t)\frac{s}{\hat{b}^2}\frac{d\hat{b}}{dt}$$

$$+ P_r^{uu}(r, s, t)\frac{r}{\hat{b}^2}\frac{d\hat{b}}{dt} + R^{+}(r, s, t) \tag{6.5.22}$$

$$P_t^{ub}(r, t) = \left[\eta\frac{\partial\hat{\theta}_S}{\partial r}\Big|_{r=1} - 2\hat{b}\theta_i(t)K\right]P^{ub}(r, t)$$

$$- P^{bb}(t)\left[\frac{r}{\hat{b}^2}\frac{d\hat{b}}{dt}\frac{\partial\hat{\theta}_S}{\partial r} + H(\hat{\theta}_S(0, t) - \theta_w)\delta(r)\right]$$

$$+ P_{rr}^{ub}(r, t) + P_s^{uu}(r, 1, t)\eta\hat{b}(t)$$

$$+ P_r^{ub}(r, t)\frac{r}{\hat{b}}\frac{d\hat{b}}{dt} - P^{uu}(r, 0, t)Q(t)P^{ub}(0, t) \tag{6.5.23}$$

$$\frac{dP^{bb}}{dt} = 2\left[\eta\frac{\partial\hat{\theta}_S}{\partial r}\Big|_{r=1} - 2\hat{b}\theta_i(t)K\right]P^{bb}(t)$$

$$+ \eta\hat{b}(t)P_r^{ub}(1, t) - P^{bu}(0, t)Q(t)P^{ub}(0, t)$$

$$+ \eta\hat{b}(t)P_s^{bu}(1, t) + R^{-1}(t) \tag{6.5.24}$$

with the symmetry condition

$$P^{ub}(r, t) = P^{bu}(r, t) \tag{6.5.25}$$

The boundary conditions are

$$\left.\begin{aligned} P_s^{uu}(r, s, t) + R_0^{-1}(t)\delta(r) &= 0 \\ P_s^{bu}(s, t) &= 0 \end{aligned}\right\} \quad s = 0 \tag{6.5.26}$$

$$\left.\begin{aligned} P_r^{uu}(r, s, t) + R_0^{-1}(t)\delta(s) &= 0 \\ P_r^{ub}(r, t) &= 0 \end{aligned}\right\} \quad r = 0 \tag{6.5.27}$$

$$\left.\begin{aligned} P^{uu}(r, s, t) &= 0 \\ P^{bu}(s, t) &= 0 \end{aligned}\right\} \quad s = 1 \tag{6.5.28}$$

$$\left.\begin{aligned} P^{uu}(r, s, t) &= 0 \\ P^{ub}(r, t) &= 0 \end{aligned}\right\} \quad r = 1 \tag{6.5.29}$$

where $R(r, s, t)$, $R(t)$, $Q(t)$, $R_0(t)$ are positive weighting factors.

These equations may appear intimidating, but it is possible to solve them through an eigenfunction expansion technique of the form

$$\hat{u}(r, t) = \sum_{n=1}^{\infty} A_n(t)\phi_n(r) \tag{6.5.30}$$

$$P^{uu}(r, s, t) = \sum_{n=1}^{\infty}\sum_{m=1}^{\infty} a_{nm}(t)\phi_n(r)\phi_m(s) \tag{6.5.31}$$

$$P^{ub}(r, t) = \sum_{n=1}^{\infty} B_n(t)\phi_n(r) \tag{6.5.32}$$

where the $\phi_n(r)$ are the eigenfunctions associated with the linear part of Eq. (6.5.18) and are the solution of

$$\ddot{\phi}(r) + \lambda_n^2\phi_n(r) = 0 \qquad 0 < r < 1 \tag{6.5.33}$$

$$\left.\begin{aligned} \dot{\phi}_n(0) &= 0 \\ \phi_n(1) &= 0 \end{aligned}\right\} \qquad n = 1, 2, \ldots \tag{6.5.34}$$

which yields

$$\left.\begin{aligned} \phi_n(r) &= \sqrt{2}\, \cos \lambda_n r \\ \lambda_n &= (2n-1)\frac{\pi}{2} \end{aligned}\right\} \qquad n = 1, 2, \ldots \tag{6.5.35}$$

Applying Galerkin orthogonality conditions to the equations for $\hat{\theta}_S$, P^{uu}, and P^{ub} yields the eigencoefficient equations

$$\dot{A}_n(t) = -\lambda_n^2 A_n(t) + c_n(t) \tag{6.5.36}$$

$$\dot{a}_{nm}(t) = -\lambda_{nm}^2 a_{nm}(t) + D_{nm}(t) \tag{6.5.37}$$

$$\dot{B}_n(t) = -\lambda_n^2 B_n(t) + E_n(t) \tag{6.5.38}$$

where $\lambda_{nm} = \sqrt{\lambda_n^2 + \lambda_m^2}$ and c_n, D_{nm}, and E_n are given by

$$\begin{aligned} c_n(t) = &-\sqrt{2}\, H\hat{b}\big(\hat{\theta}_s(0, t) - \theta_w\big) - 2\frac{d \ln \hat{b}}{dt}\sum_{m=1}^{N} A_m(t)\lambda_m I_{nm} \\ &+ \sqrt{2}\, Q(t)(y - \hat{\theta}(0, t)) \sum_{m=1}^{N_c} a_{nm} \end{aligned} \tag{6.5.39}$$

$$D_{nm}(t) = B_n\left[-2\sqrt{2}\,H\big(\hat{\theta}_S(0,t)-\theta_w\big) + \frac{2}{\hat{b}^2}\frac{d\hat{b}}{dt}\left(\sum_{j=1}^{N}\lambda_j A_j I_{jm}\right)\right]$$

$$+ B_m\left[-2\sqrt{2}\,H\big(\hat{\theta}_S(0,t)-\theta_w\big) + \frac{2}{\hat{b}^2}\frac{d\hat{b}}{dt}\left(\sum_{k=1}^{N}\lambda_k A_k I_{kn}\right)\right]$$

$$-2\frac{d\ln\hat{b}}{dt}\left(\sum_{k=1}^{N_c} a_{km}\lambda_k I_{mk} + \sum_{j=1}^{N_c} a_{nj}\lambda_j I_{nj}\right)$$

$$-2Q(t)\sum_{k=1}^{N_c} a_{nk}\sum_{j=1}^{N_c} a_{jm} + \frac{2R^{+}(-1)^{m+1}(-1)^{n+1}}{\lambda_m\lambda_n}$$

$$+ R_0^{-1}\left(\frac{(-1)^{n+1}}{\lambda_n} + \frac{(-1)^{m+1}}{\lambda_m}\right) \tag{6.5.40}$$

$$E_n(t) = \frac{2}{\hat{b}^2}P^{bb}(t)\frac{d\hat{b}}{dt}\sum_{j=1}^{N} A_j\lambda_j I_{jn} - \sqrt{2}\,P^{bb}H\big(\hat{\theta}_S(0,t)-\theta_w\big)$$

$$-2\frac{d\ln\hat{b}}{dt}\sum_{k=1}^{N_c}\lambda_k B_k I_{kn}$$

$$-\left(\sqrt{2}\,\eta\sum_{m=1}^{N}\lambda_m A_m(-1)^{m+1} + 2\hat{b}\theta_l K\right)B_n - 2Q(t)\sum_{k=1}^{N_c} B_k\sum_{m=1}^{N_c} a_{nm} \tag{6.5.41}$$

The variables $\hat{b}(t)$ and $P^{bb}(t)$ may be determined from

$$\frac{d\hat{b}}{dt} = -\eta\hat{b}\sqrt{2}\sum_{m=1}^{N}(-1)^{m+1}\lambda_m A_m(t)$$

$$-\hat{b}^2K\theta_l + \sqrt{2}\left(\sum_{k=1}^{N_c} B_k\right)Q(t)\big(y-\hat{\theta}_S(0,t)\big) \tag{6.5.42}$$

$$\frac{dP^{bb}}{dt} = -2P^{bb}\left[\eta\sqrt{2}\sum_{m=1}^{N}(-1)^{m+1}\lambda_m A_m(t) + 2\hat{b}\theta_l K\right]$$

$$+2\sqrt{2}\,\eta\hat{b}\sum_{k=1}^{N_c}(-1)^{k+1}\lambda_k B_k(t)$$

$$-\left(\sum_{i=1}^{N_c} B_i(t)\right)Q(t)\left(\sum_{j=1}^{N_c} B_j(t)\right) + R^{-1}(t) \tag{6.5.43}$$

Here N is the number of eigenfunctions required for the filter estimates, while N_c is the number of eigenfunctions used to represent the differential sensitivities. The state estimation algorithm then consists of solving $N + 1$ ordinary differential equations for the filter [Eqs. (6.5.36) and (6.5.42)] and

$1 + N_c + (N_c^2 + N_c)/2$ ordinary differential equations for the differential sensitivities [Eqs. (6.5.37), (6.5.38), and (6.5.43)]. Although it would be possible to solve both the filter and sensitivity equations in real time, in practice it is more practical to solve the sensitivity equations in an approximate way off-line for a nominal state trajectory so that only the $N + 1$ filter equations need be integrated in real time. In this way the state estimator is easily implemented in real time on presently available process control computers. In the present study, it was found (after some adjustments in the computational procedure [6]) that $N = 4$ was sufficient to provide a good solution to the filter equations and $N_c = 3$ sufficed for adequate filter performance. Thus the filter required the solution of five ordinary differential equations in real time. In order to provide an initial test of the filter in the face of large measurement errors, a number of simulations were performed. The steel surface temperature measurement "data" were provided by a simulation of the model in which the resulting surface temperatures $\theta_S(0, t)$ were corrupted by adding zero-mean white Gaussian noise from a random number generator having a specified standard deviation σ.

A selection of results may be seen in Figs. 6.35 to 6.38 for the filter parameters given in Table 6.3. As can be seen, this nonlinear filter performs well, converging from extremely poor initial guesses in a very short time even in the face of 100°C standard deviation measurement error.

Evaluation

Although the state estimation algorithm developed here has been tested only through simulation, these tests show that minimal real-time computations are required for implementation and indicate that the solid steel crust thickness can be adequately tracked by the estimator. Further experimental testing of the estimator and evaluation of feedback controllers for casting operations is reported elsewhere [6, 7].

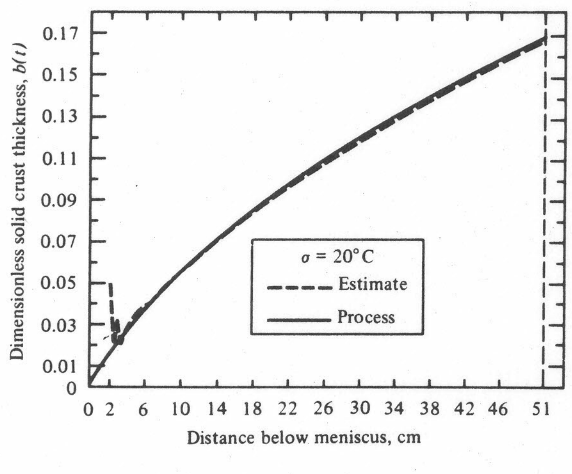

Figure 6.35 Filter estimates and process behavior for the solid crust thickness, σ = 20°C.

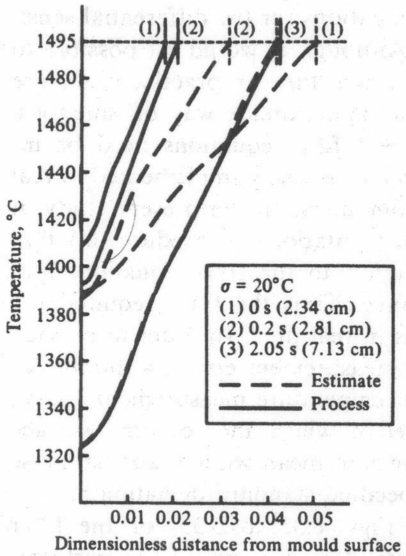

Figure 6.36 Filter estimates and process behavior for the temperature profile in the solid crust, $\sigma = 20°C$.

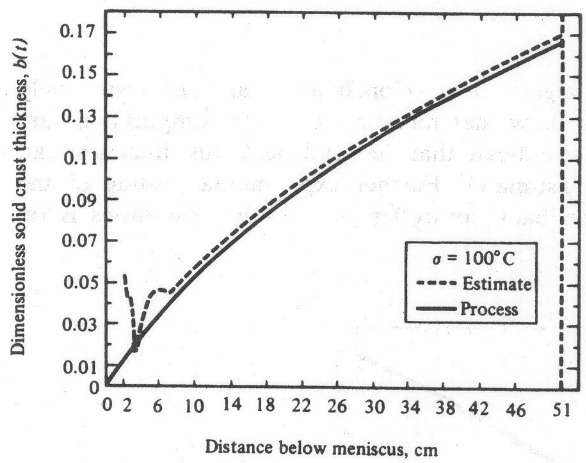

Figure 6.37 Filter estimates and process behavior for the solid crust thickness, $\sigma = 100°C$.

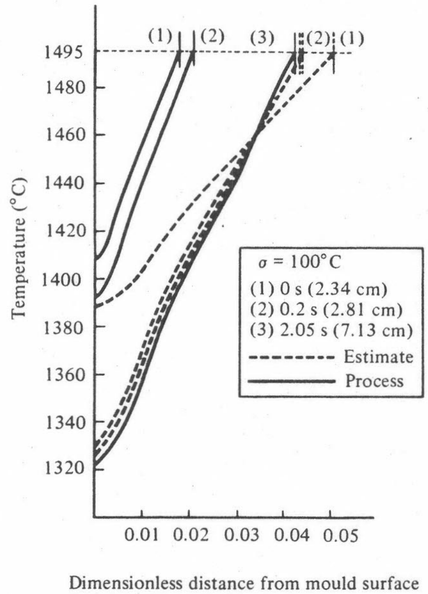

Figure 6.38 Filter estimates and process behavior for the temperature profile in the solid crust, $\sigma = 100°C$.

Table 6.3 Filter parameters

Figure no.	σ	$Q(t)$	$P^{bb}(0)$
6.35–6.36	20°C	1.96	0.001
6.37–6.38	100°C	0.0784	0.007

For all runs: $\hat{b}(0) = 0.05$, $R^{-1} = R_0^{-1} = R^+ = 0$, $B_n(0) = 0$, $D_{nm}(0) = 1.02/\lambda_n\lambda_m$.

6.6 FURTHER CASE STUDIES

A number of other case studies which have appeared in the literature recently illustrate the application of modern process control to industrial scale or pilot plant processes. These include studies on distillation column control, chemical reactor control, paper mill control, steel mill control, and a wide range of other process control problems [8–12]. The reader is urged to consult these references and the current journal literature for further examples.

REFERENCES

1. Fisher, D. G., and D. E. Seborg: *Multivariable Computer Control—A Case Study*, American Elsevier, New York, 1976.
2. Lausterer, G. K., W. H. Ray, and H. R. Martens: *Automatica*, **14**:335 (1978).
3. Lausterer, G. K., and W. H. Ray: *IEEE Trans. Auto. Control*, **AC-24**:179 (1979).

4. Lausterer, G. K., Ph.D. thesis, State University of New York at Buffalo, 1977.
5. Greiss, F. K., and W. H. Ray: *Proc. IFAC Symp. New Trends Sys. Anal.*, Springer-Verlag, 1977.
6. Greiss, F. K.: Ph.D. thesis, University of Wisconsin, 1978.
7. Greiss, F. K., and W. H. Ray: *Automatica*, **16** (1980).
8. Foss, A. S., and M. M. Denn: "Chemical Process Control," AIChE. Symposium Series 72 (1976).
9. *Proc. Joint Autom. Control Conf.*, 1976–1979.
10. Lemke, H., R. Van Nauta, and H. B. Verbruggen (eds.): *Digital Computer Applications to Process Control*, North-Holland, Amsterdam, 1977.
11. Ray, W. H.: *Automatica*, **14**:281 (1978).
12. Ray, W. H., and D. G. Lainiotis (eds.): *Distributed Parameter Systems*, Marcel Dekker, New York, 1978.

APPENDIX

SOME COMPUTER-AIDED DESIGN PROGRAMS

A number of educational and research institutions have devoloped computer-aided design programs for interactive computer-aided control system design [1]. Some of the more comprehensive design packages are listed in the table below. These computer programs are usually available for a fee. Further information may be obtained directly from the sources given.

Program	Capabilities	Source
1. CYPROS, DAREK	For linear and nonlinear lumped parameter systems: 1. Optimal and suboptimal multivariable feedback control 2. Process identification 3. State estimation 4. Simulation	Division of Engineering Cybernetics Technical University of Norway Trondheim, Norway
2. UMIST COMPUTER-AIDED CONTROL-SYSTEM DESIGN SUITE	For linear lumped parameter systems: 1. Optimal and suboptimal multivariable feedback control 2. State estimation 3. Simulation	Control Systems Centre University of Manchester Institute of Science and Technology Manchester, England
3. CAMBRIDGE LINEAR ANALYSIS DESIGN PROGRAMS	For linear lumped parameter systems: 1. Multivariable feedback control 2. Simulation	Control Engineering Dept. Cambridge University Cambridge, England
4. GEMSCOPE	For linear lumped parameter systems: 1. Optimal and suboptimal feedback control 2. State estimation 3. Simulation	Data Acquisition and Control System Center Dept. of Chemical Eng. University of Alberta Edmonton, Alberta Canada

REFERENCE

1. Lemmens, W. J. M., and A. J. W. Van den Boom: *Automatica*, **15**:113 (1979).

INDEXES

AUTHOR INDEX

SUBJECT INDEX